日本磁気学会
ISSN 2432-0250
Journal of the Magnetics Society of Japan
Electronic Journal URL: https://www.jstage.jst.go.jp/browse/msjmag

Vol.48 No.3　2024

Journal

JOURNAL OF THE MAGNETICS SOCIETY OF JAPAN

Vol.48 No.3 2024

日本磁気学会

ISSN 2432-0250

HP: http://www.magnetics.jp/ e-mail: msj@bj.wakwak.com

Electronic Journal: http://www.jstage.jst.go.jp/browse/msjmag

TPM-2-08s25

HcJの3σ/Ave. 0.2%※1を実現
渦電流補正方法※2も確立済

試料測定磁界	最大試料直径
max 15 Tesla	10mm

パルス励磁型磁気特性測定装置

永久磁石および磁性体粉末を固形化した高磁化試料のヒステリシス曲線の自動測定および描画、SPD(Singuler Point Detection) 測定が可能です。(RT～+200℃)

※1 電気学会資料 MAG-18-088 参照
※2 電気学会資料 MAG-07-011 参照

NdFeB(sintered) 測定例

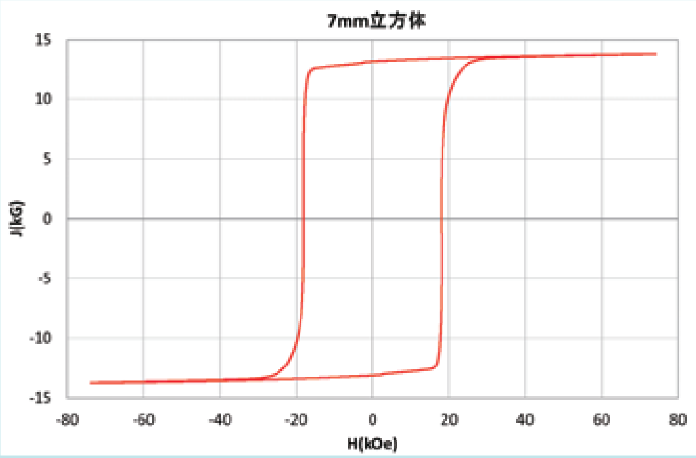

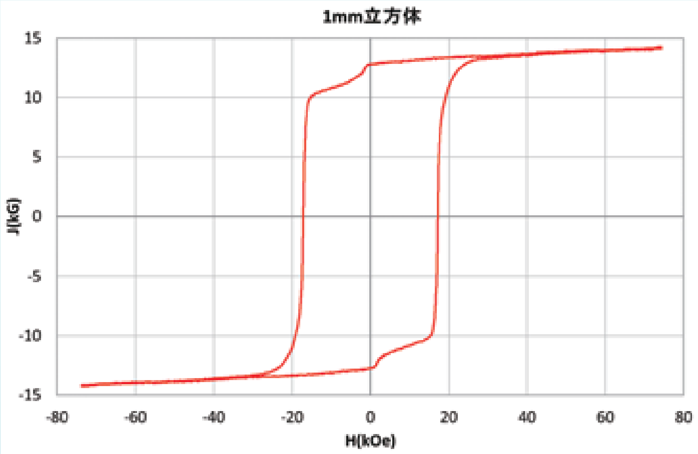

1mm 立方体測定用検出コイルはオプション品です

東英工業では他に振動試料型磁力計(VSM)、直流自記磁束計(JIS C2501 準拠)を始め、

各種磁気測定装置を取り揃えております。ぜひお問い合わせ下さい

TOEI 東英工業株式会社
http://www.toeikogyo.co.jp
〒194-0035 東京都町田市忠生1-8-13
TEL:042-791-1211 FAX:042-792-0490
E-mail:sales@toeikogyo.co.jp

Journal of the Magnetics Society of Japan
Vol. 48, No. 3

Electronic Journal URL: https://www.jstage.jst.go.jp/browse/msjmag

CONTENTS

INDEX

J. Magn. Soc. Jpn., **48**, 40-46 (2024) <Paper>

Influence of Design Parameters on Adjacent Track Interference in Heated-Dot Magnetic Recording

T. Kobayashi and I. Tagawa*

Graduate School of Engineering, Mie Univ., *1577 Kurimamachiya-cho, Tsu 514-8507, Japan*

*Electrical and Electronic Engineering, Tohoku Institute of Technology, *35-1 Yagiyama-Kasumicho, Sendai 982-8577, Japan*

We discuss the influence of design parameters on adjacent track interference (ATI) in 4 Tbpsi heated-dot magnetic recording where the parameters are the mean Curie temperature, Curie temperature variation, anisotropy constant ratio, dot size variation, Gilbert damping constant, writing field magnitude, and writing field angle. We calculate the dot height to achieve a bit error rate of 10^{-3} after adjacent track writing as a function of the design parameters. The dot height must be increased when we choose a lower mean Curie temperature, since the thermal gradient decreases simultaneously. The adjacent track temperature is related to the Curie temperature variation via the writing temperature. ATI is strongly affected by the anisotropy constant ratio. The dot height must be increased as the dot size variation increases, since the probability of a small dot appearing increases. The Gilbert damping constant has an effect on ATI. Since a writing field magnitude of 10 kOe is relatively small against the anisotropy field, the increase in the dot height is relatively small when the writing field magnitude increases from 10 to 15 kOe or the writing field angle changes from 180 to 135 deg.

Key words: HDMR, ATI, mean Curie temperature, Curie temperature variation, anisotropy constant ratio, dot size variation, Gilbert damping constant, writing field magnitude, writing field angle

1. Introduction

Many magnetic recording methods have been proposed to solve the trilemma problem[1] of conventional magnetic recording (CMR) on granular media. These methods include shingled magnetic recording (SMR), microwave-assisted magnetic recording (MAMR), heat-assisted magnetic recording (HAMR), bit patterned media (BPM), and three-dimensional magnetic recording (3D MR).

The challenges facing the design of MR media are
(1) information stability during 10 years of archiving, known as the $K_uV/(kT)$ problem[1], where K_u, V, k, and T are respectively the grain or dot anisotropy constant, volume, Boltzmann constant, and temperature,
(2) information stability in an adjacent track during writing, known as the adjacent track interference (ATI) problem, and
(3) the writing field dependence of the bit error rate (bER), namely writability.

Micromagnetic calculation is useful for examining (2) in SMR and (3). However, this is not practical due to the long calculation time required for subjects (1) and (2) in CMR because of the 10^3-10^4 times rewrite in the adjacent track. We have proposed a model calculation employing the Néel-Arrhenius model with a Stoner-Wohlfarth grain or dot. This model is applicable to all three subjects[2] including SMR and CMR.

The above three subjects, namely (1), (2), and (3), must be dealt with simultaneously, since they are in a trade-off relationship. For example, if the design parameter of the anisotropy constant ratio is larger, the information in (1) and (2) is more stable, but (3) the writability will be worse even for HAMR. The anisotropy constant ratio K_u/K_{bulk}, which we introduced[3], is the intrinsic ratio of the medium anisotropy constant to the bulk FePt anisotropy constant. The K_u/K_{bulk} value is independent of the Curie temperature T_c, and is constant for any temperature from zero Kelvin to T_c. The design parameters are related to each other in a complex manner. It is necessary to examine the influence of the design parameters on the above three subjects when designing the medium.

Akagi *et al.* reported (3) the recording performance of heated-dot magnetic recording (HDMR)[4], namely HAMR on BPM, employing micromagnetic calculation. We have previously discussed information stability (1) during 10 years of archiving and (2) during adjacent track (AT) writing for HDMR[5] employing our model calculation, in which we have calculated the dot height to achieve a bER of 10^{-3} after AT writing as a function of the thermal gradient for the cross-track direction.

In this paper, as a first step in examining the trade-off relationship between (2) ATI and (3) the writability, we discuss the influence of the design parameters on (2) ATI in 4 Tbpsi HDMR where the parameters are the mean Curie temperature, Curie temperature variation, anisotropy constant ratio, dot size variation, Gilbert damping constant, writing field magnitude, and writing field angle. We calculate the dot height to achieve a bit error rate of 10^{-3} after adjacent track writing as a function of the design parameters.

Corresponding author: T. Kobayashi (e-mail: kobayasi @phen.mie-u.ac.jp).

2. Calculation Condition and Method

2.1 Dot arrangement and medium structure

Figure 1 shows the dot arrangement and medium structure in 4 Tbpsi HDMR where D_x, D_y, and h are the dot sizes for the down-track and cross-track directions, and the dot height, respectively. The bit length D_{B} and track width D_{T} were both 12.7 nm. We assumed that the mean dot size D_{m} and mean dot spacing Δ_{D} are the same for both the down-track and cross-track directions, namely $D_{\mathrm{m}} = \Delta_{\mathrm{D}} = 6.35$ nm. The h values were 5.1 and 2.8 nm for the standard values in conventional and shingled HDMR, respectively.

There are two cases for the dot sizes D_x and D_y according to the dot manufacturing method. (1) In one case, the D_x and D_y sizes are the same, and the $D_x = D_y$ size fluctuates. (2) Another case is that the D_x and D_y sizes fluctuate independently. We examined (1) the $D_x = D_y$ case, since the bER is larger for the same h value[5]. We generated a random number $D_x = D_y$ according to a log-normal distribution with a standard deviation σ_{D}. We used a $\sigma_{\mathrm{D}}/D_{\mathrm{m}}$ value of 15 % for the standard value.

2.2 Magnetic properties

The temperature dependence of the medium magnetization M_{s} was calculated by employing mean field analysis[6], and that of the K_{u} value was assumed to be proportional to M_{s}^2[7]. $M_{\mathrm{s}}(T_{\mathrm{c}} = 770\ \mathrm{K}, T = 300\ \mathrm{K}) = 1000$ emu /cm^3 was assumed for FePt. Based on this assumption, the M_{s} value can be calculated for all values of T_{c} and T.

$K_{\mathrm{u}}(T_{\mathrm{c}} = 770\ \mathrm{K}, K_{\mathrm{u}}/K_{\mathrm{bulk}} = 1, T = 300\ \mathrm{K}) = 70$ Merg/cm^3 was assumed for bulk FePt. Using this assumption, we can calculate K_{u} for all values of T_{c}, $K_{\mathrm{u}}/K_{\mathrm{bulk}}$, and T. No intrinsic distribution of K_{u} was assumed. However, there was a fluctuation in K_{u} caused by T_{c} variation.

The T_{c} value of each dot can be adjusted by changing the Cu composition z for $(\mathrm{Fe}_{0.5}\mathrm{Pt}_{0.5})_{1-z}\mathrm{Cu}_z$.

With a T_{c} value of 750 K and a $K_{\mathrm{u}}/K_{\mathrm{bulk}}$ value of 0.8, in this work we obtain a K_{u} value of 51 Merg/cm^3 and an anisotropy field H_{k} of 107 kOe at a readout temperature of 330 K.

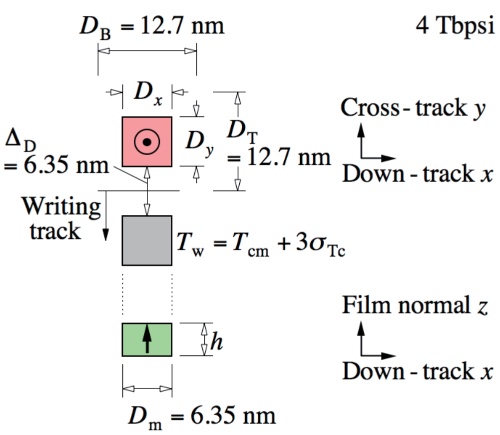

Fig. 1 Dot arrangement and medium structure.

2.3 Temperature profile

The writing temperature T_{w} for the dot was assumed to be

$$T_{\mathrm{w}} = T_{\mathrm{cm}} + 3\sigma_{\mathrm{Tc}} \tag{1}$$

as shown in Fig. 1 where T_{cm} and σ_{Tc} are the mean Curie temperature and the standard deviation of T_{cm}, respectively, taking account of the T_{c} variation. The T_{c} distribution was assumed to be normal. Based on this assumption, 99.9 % of dots in the writing track are heated to above their T_{c} values during the writing period. We used T_{cm} and $\sigma_{\mathrm{Tc}}/T_{\mathrm{cm}}$ values of 750 K and 2 %, respectively, for the standard values.

For simplicity, the thermal gradient $\mathrm{d}T/\mathrm{d}y$ in the cross-track direction was assumed to be constant anywhere. The thermal gradient in the down-track direction was zero, since the exposure time for writing has little effect on the results as shown below in 3.1. Since the $\mathrm{d}T/\mathrm{d}y$ value can be adjusted by changing the medium structure, we used a $\mathrm{d}T/\mathrm{d}y$ value of 14 K/nm for the standard value.

When the T_{cm} value decreases from high Curie temperature T_{cmH} to low T_{cmL}, the thermal gradients also decrease from $\mathrm{d}T_{\mathrm{H}}(y)/\mathrm{d}y$ to $\mathrm{d}T_{\mathrm{L}}(y)/\mathrm{d}y$ as explained below. If the medium structure is the same, the difference between the medium temperature $T_i(y)$ and ambient temperature T_{amb} is proportional to the laser power $P_{\mathrm{w}i}$ for heating regardless of the medium position y where $i = \mathrm{H}$ for media with T_{cmH} and $i = \mathrm{L}$ for T_{cmL}. Therefore, we can obtain the following equation.

$$\frac{T_{\mathrm{L}}(y)-T_{\mathrm{amb}}}{T_{\mathrm{H}}(y)-T_{\mathrm{amb}}} = \frac{P_{\mathrm{wL}}}{P_{\mathrm{wH}}}.$$

Since at the center of the track,

$$\frac{T_{\mathrm{L}}(y)-T_{\mathrm{amb}}}{T_{\mathrm{H}}(y)-T_{\mathrm{amb}}} = \frac{T_{\mathrm{wL}}-T_{\mathrm{amb}}}{T_{\mathrm{wH}}-T_{\mathrm{amb}}} = \frac{T_{\mathrm{cmL}}+3\sigma_{\mathrm{TcL}}-T_{\mathrm{amb}}}{T_{\mathrm{cmH}}+3\sigma_{\mathrm{TcH}}-T_{\mathrm{amb}}},$$

$$T_{\mathrm{L}}(y) - T_{\mathrm{amb}} = \frac{T_{\mathrm{cmL}}+3\sigma_{\mathrm{TcL}}-T_{\mathrm{amb}}}{T_{\mathrm{cmH}}+3\sigma_{\mathrm{TcH}}-T_{\mathrm{amb}}} \cdot (T_{\mathrm{H}}(y) - T_{\mathrm{amb}}),$$

we can obtain

$$\frac{\mathrm{d}T_{\mathrm{L}}(y)}{\mathrm{d}y} = \frac{T_{\mathrm{cmL}}+3\sigma_{\mathrm{TcL}}-T_{\mathrm{amb}}}{T_{\mathrm{cmH}}+3\sigma_{\mathrm{TcH}}-T_{\mathrm{amb}}} \cdot \frac{\mathrm{d}T_{\mathrm{H}}(y)}{\mathrm{d}y},$$

$$= \frac{T_{\mathrm{cmL}}(1+3\times0.02)-330}{750\times(1+3\times0.02)-330} \times 14, \tag{2}$$

for $T_{\mathrm{cmH}} = 750$ K, where T_{wH} and T_{wL} are the writing temperatures for media with T_{cmH} and T_{cmL}, respectively, and σ_{TcH} and σ_{TcL} are the standard deviations for media with T_{cmH} and T_{cmL}, respectively. We assumed that the T_{amb} value was 330 K.

Although we do not deal the dependence of the T_{c} variation on the Cu composition in this paper, we point out this in the following, since this will be important in actual HAMR and HDMR. When a third element is

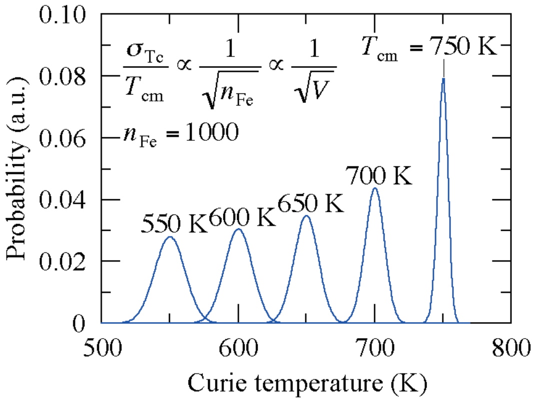

Fig. 2 Curie temperature distribution for various mean Curie temperatures $T_{\rm cm}$.

added to FePt to reduce its $T_{\rm cm}$, some dots contain more or less atoms of a third element than a mean number. Reducing $T_{\rm cm}$ by adding a third element intrinsically results in $T_{\rm c}$ variation and the $T_{\rm c}$ variation may lead to an increase in bER. Figure 2 shows the $T_{\rm c}$ distribution for various $T_{\rm cm}$ values, in which the third element variation was calculated statistically and $T_{\rm c}$ was calculated by employing mean field analysis for an Fe site number $n_{\rm Fe}$ of 1000 in a dot. The $T_{\rm c}$ distribution of course becomes zero for FePt ($T_{\rm c} \approx 770$ K) with no third element. The $T_{\rm c}$ variation increases as the third element number increases and the $T_{\rm cm}$ value decreases. The $T_{\rm c}$ standard deviation $\sigma_{\rm Tc}$ is inversely proportional to $\sqrt{n_{\rm Fe}}$, namely $\sqrt{V}$. We used a $\sigma_{\rm Tc}/T_{\rm cm}$ value of 2 % for the standard value. This problem is a subject for future study.

2.4 ATI evaluation method

The information stability for 10 years of archiving has been discussed employing the Néel-Arrhenius model with a Stoner-Wohlfarth grain or dot. The attempt period $1/f_0$ has a value in picoseconds for FePt in heat-assisted magnetic recording. Since the magnetization direction attempts to reverse with a certain probability at each attempt period, the information stability for 10 years of archiving is extrapolated as a stack of phenomena in picoseconds. Therefore, the Néel-Arrhenius model is valid for any time from the order of a picosecond to more than 10 years. Therefore, we have also applied the Néel-Arrhenius model to phenomena with a short time, and examined information stability during AT writing.

The magnetization reversal number Nt for the dot from time 0 to t is expressed as

$$Nt = f_0 t \exp(-K_\beta), \tag{3}$$

employing the Néel-Arrhenius model where f_0 is the attempt frequency[8]. We assumed f_0 as

$$f_0 = \frac{\gamma\alpha}{1+\alpha^2}\sqrt{\frac{M_{\rm s}H_{\rm keff}^3 V}{2\pi kT}}\left(1+\frac{|H_{\rm w}|\cos\phi}{H_{\rm keff}}\right)\left(1-\left(\frac{|H_{\rm w}|\cos\phi}{H_{\rm keff}}\right)^2\right), \tag{4}$$

taking account of the effective anisotropy field $H_{\rm keff}$ and writing field angle ϕ as shown in Fig. 3 where γ, α, $V = D_x D_y \times h$, and $|H_{\rm w}|$ are respectively the gyromagnetic ratio, Gilbert damping constant, dot volume, and writing field magnitude. K_β is the thermal stability factor given by

$$K_\beta = \frac{E_1 - E_0}{kT}, \tag{5}$$

where $E_1 - E_0$ is the energy barrier. The $f_0 t$ value gives an attempt number for magnetization reversal, and the Boltzmann factor $\exp(-K_\beta)$ is interpreted as the probability of magnetization reversal.

We have reported an approximate equation[9] for $E_1 - E_0$ in the Stoner-Wohlfarth dot for angles ϕ of 0 to 180 deg, taking account of Pfeiffer's approximation[10] and shape anisotropy energy. When $|H_{\rm w}| = 0$, $E_1 - E_0$ becomes $K_{\rm ueff}V$ where $K_{\rm ueff}$ is the effective anisotropy constant, taking account of the shape anisotropy. The approximate equations for $0 \le \phi \le 90$ deg are summarized as follows,

$$\frac{E_1 - E_0}{K_{\rm ueff}V} = \left(1 + 2\left(\cos\phi - \frac{1}{2}\right)\frac{|H_{\rm w}|/H_{\rm keff}}{H_{\rm sw}/H_{\rm keff}}\right)^x,$$

$$(|H_{\rm w}|/H_{\rm keff} \le H_{\rm sw}/H_{\rm keff})$$

$$x = 2.0(H_{\rm sw}/H_{\rm keff}), \tag{6}$$

and for $90 \le \phi \le 180$ deg,

$$\frac{E_1 - E_0}{K_{\rm ueff}V} = \left(1 - \frac{|H_{\rm w}|/H_{\rm keff}}{H_{\rm sw}/H_{\rm keff}}\right)^x,$$

$$(|H_{\rm w}|/H_{\rm keff} \le H_{\rm sw}/H_{\rm keff})$$

$$x = 0.86 + 1.14(H_{\rm sw}/H_{\rm keff}), \tag{7}$$

where

$$K_{\rm ueff} = K_{\rm u} + \frac{(4\pi - 3N_z)M_{\rm s}^2}{4}, \tag{8}$$

$$N_z = 8\arctan\left(\frac{D_x D_y}{h\sqrt{D_x^2 + D_y^2 + h^2}}\right), \tag{9}$$

$$H_{\rm keff} = \frac{2K_{\rm ueff}}{M_{\rm s}}, \tag{10}$$

$$\frac{H_{\rm sw}}{H_{\rm keff}} = \frac{1}{(|\sin\phi|^{2/3} + |\cos\phi|^{2/3})^{3/2}}. \tag{11}$$

$H_{\rm sw}$ and N_z are respectively the magnetization switching field and demagnetizing factor.

The dot error probability P from time 0 to t is well-known as

$$P = 1 - \exp\left(-f_0 t \exp(-K_\beta)\right). \tag{12}$$

If $f_0 t \exp(-K_\beta) \ll 1$, Eq. (12) becomes

$$P = Nt = f_0 t \exp(-K_\beta). \tag{13}$$

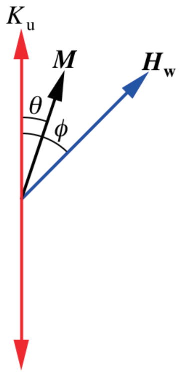

Fig. 3 Definition of angles of magnetization $\boldsymbol{M}$ and writing field $\boldsymbol{H}_w$ vectors.

Table 1 Standard calculation conditions.

Recording density (Tbpsi)	4
Bit length D_B (nm)	12.7
Track width D_T (nm)	12.7
Mean dot size D_m (nm)	6.4
Standard deviation σ_D / D_m (%)	15
Mean dot spacing Δ_D (nm)	6.4
Dot height h (nm) (conventional HDMR)	5.1
Dot height h (nm) (shingled HDMR)	2.8
Exposure time t (μs) (conventional HDMR)	1
Exposure time t (ns) (shingled HDMR)	1
Mean Curie temperature T_{cm} (K)	750
Standard deviation σ_{Tc} / T_{cm} (%)	2
Anisotropy constant ratio K_u / K_{bulk}	0.8
Gilbert damping constant α	0.1
Writing field magnitude $\lvert H_w \rvert$ (kOe)	10
Writing field angle ϕ (deg)	180
Storage temperature T_{sto} (K)	350

Although the bER value is calculated using the P values of the grains in a bit for HAMR, the bER value is equal to the P value for HDMR, since 1bit consists of 1 dot.

The criterion determining whether or not information is stable was assumed to be a bER of 10^{-3}. The bER in this paper is useful only for comparisons.

The standard calculation conditions are summarized in Table 1. We used an exposure time t of 1 μs for writing in conventional HDMR, taking account of 10^3 times rewrite. A t value of 1 ns was used in shingled HDMR. The $|H_w|$ and ϕ values were 10 kOe and 180 deg, respectively.

3. Calculation Results

3.1 Mean Curie temperature

The T_{cm} dependence of the bER after AT writing is shown in Fig. 4 (a). A t value of 1 ns was used in shingled HDMR. However, the results for 1 ns and 0.5 ns are almost the same, since t is not a variable of the exponential function as shown in Eq. (13).

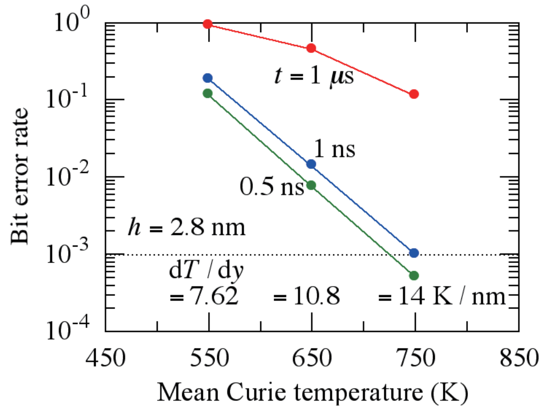

(a)

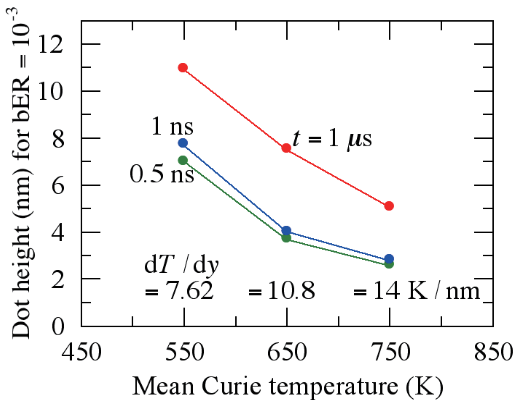

(b)

Fig. 4 (a) Bit error rate (bER) as a function of mean Curie temperature T_{cm} after adjacent track (AT) writing for various exposure times t for writing and (b) dot height h to achieve a bER of 10^{-3} as a function of mean Curie temperature T_{cm}.

The AT temperature T_{adj} can be calculated as

$$T_{adj} = T_{cm} + 3\sigma_{Tc} - D_T \frac{dT}{dy}, \qquad (14)$$

where D_T is the track width. We assumed a dT/dy value of 14 K/nm for $T_{cm} = 750$ K and lowered the dT/dy value indicated in Fig. 4 according to Eq. (2) as the T_{cm} value decreased. We adjusted the h value to 2.8 nm so that the bER value reached 10^{-3} for $T_{cm} = 750$ K and $t = 1$ ns as shown in Fig. 4 (a). As a result, the bER value increases when we choose the lower T_{cm} value, since the temperature difference $T_{cm} - T_{adj}$ decreases from 133 to 98 and 64 K as the dT/dy value decreases from 14 to 10.8 and 7.62 K/nm, respectively. The T value is a parameter with considerable impact, since T is a variable of the exponential function via K_β.

Figure 4 (b) shows the h value needed to achieve a bER of 10^{-3} after AT writing as a function of T_{cm}. The h value must be increased strongly as the T_{cm} value decreases, since the T_{cm} and dT/dy values are closely related to each other.

3.2 T_c standard deviation

Figure 5 shows the h value as a function of σ_{Tc}/T_{cm} for T_{cm} = 750 K. When the σ_{Tc}/T_{cm} value increases, the probability of a low T_c dot appearing increases. Furthermore, the T_w and dT/dy values increase as the σ_{Tc}/T_{cm} value increases according to Eqs. (1) and (2), respectively. The resultant T_{adj} value calculated with Eq. (14) increases as the σ_{Tc}/T_{cm} value increases as indicated in Fig. 5. Therefore, the h value must be increased as the σ_{Tc}/T_{cm} value increases.

3.3 Anisotropy constant ratio

We also examined the K_u/K_{bulk} dependence of h. When K_u/K_{bulk} is halved from 0.8 to 0.4, K_{ueff} is also almost halved, since the shape anisotropy energy is small. Furthermore, H_{keff} is almost halved and the K_β value is reduced by less than half as

$$K_\beta = \frac{K_{ueff}V}{kT}\left(1 - \frac{|H_w|}{H_{keff}}\right)^2. \qquad (15)$$

Therefore, the h value for a bER of 10^{-3} must be more than doubled for a decrease in the K_u/K_{bulk} value from 0.8 to 0.4 as shown in Fig. 6.

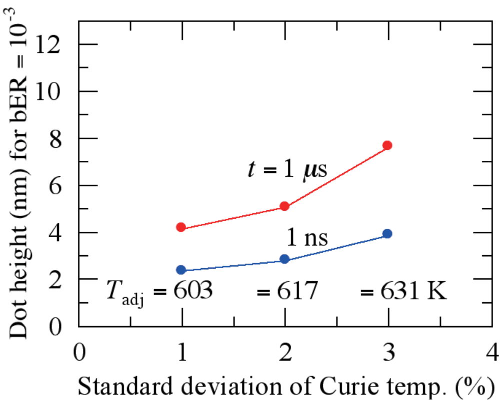

Fig. 5 Dot height h to achieve a bER of 10^{-3} as a function of the standard deviation σ_{Tc}/T_{cm} of the Curie temperature after AT writing.

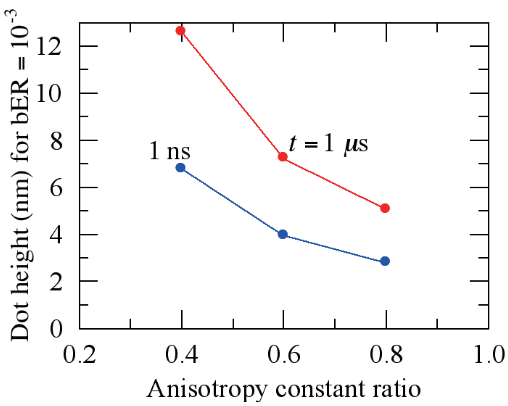

Fig. 6 Dot height h to achieve a bER of 10^{-3} as a function of anisotropy constant ratio K_u/K_{bulk} after AT writing.

3.4 Dot size variation

When the σ_D/D_m value increases, the probability of a small dot appearing increases. Therefore, the h value must be increased as the σ_D/D_m value increases as shown in Fig. 7.

3.5 Gilbert damping constant

The P value is determined by f_0 and K_β as shown in Eq. (13). If the f_0 value becomes 10 times larger, the K_β

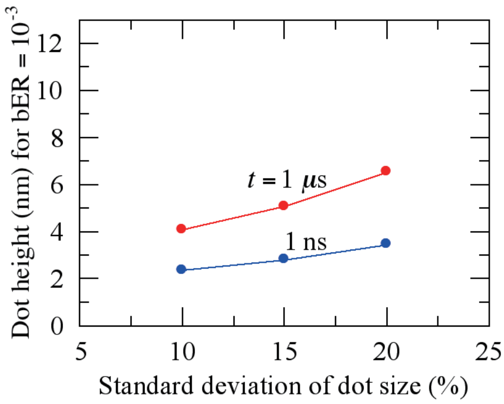

Fig. 7 Dot height h to achieve a bER of 10^{-3} as a function of the standard deviation σ_D/D_m of the dot size after AT writing.

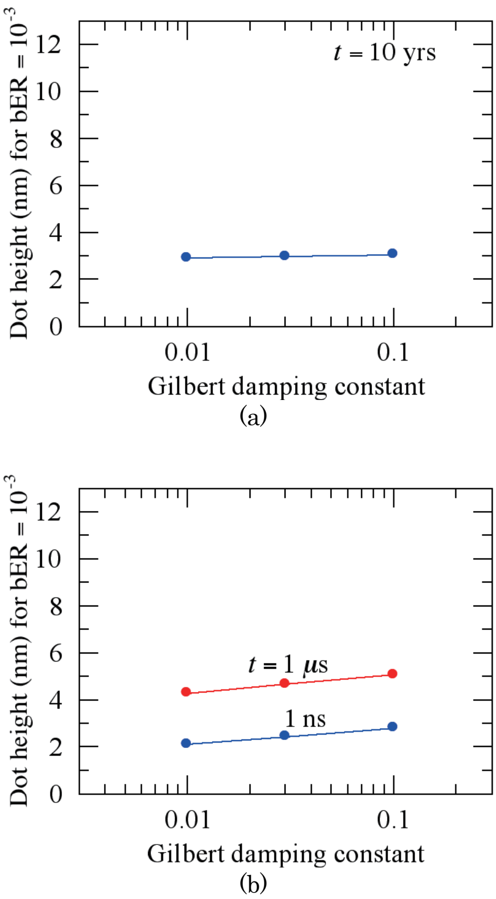

Fig. 8 Dot height h to achieve a bER of 10^{-3} as a function of the Gilbert damping constant α after (a) 10 years of archiving and (b) AT writing.

value must increase by 2.3 to obtain the same Nt value as

$$f_0 \exp(-K_\beta) = 10\, f_0 \exp(-K_\beta'),$$

$$K_\beta' = K_\beta + \ln(10) \approx K_\beta + 2.3. \qquad (16)$$

Furthermore, the α value is considered to be smaller than 0.1. Therefore, f_0 is almost proportional to α, since

$$f_0 \propto \frac{\alpha}{1+\alpha^2}. \qquad (17)$$

We assumed the storage temperature T_{sto} to be 350 K for 10 years of archiving. We took a certain margin into account. The value of K_β is around 120 at T_{sto}, and that is much larger than the value of 2.3 seen in Eq. (16). Therefore, the α value has little effect on 10 years of archiving as shown in Fig. 8 (a). However, since the K_β value becomes small due to the temperature increasing to 617 K during AT writing, the α value has an effect on ATI as shown in Fig. 8 (b).

3.6 Writing field magnitude

Figure 9 shows the h value as a function of $|H_{\mathrm{w}}|$. The K_β value decreases as the $|H_{\mathrm{w}}|$ value increases according to Eq. (15) where the H_{keff} value is about 67 kOe. Therefore, the h value must be increased as the $|H_{\mathrm{w}}|$ value increases.

3.7 Writing field angle

When ϕ decreases from 180 to 135 deg, the H_{sw} value is halved from 1.0 to 0.5 according to Eq. (11). Then the K_β value decreases according to Eqs. (5) and (7), and the h value must be increased as shown in Fig. 10 (a). Figure 10 (b) shows the $(E_1 - E_0)/(K_{\mathrm{ueff}}V)$ value as a function of $|H_{\mathrm{w}}|/H_{\mathrm{keff}}$ for various ϕ values. Although the H_{sw} value is halved, the decrease of $(E_1 - E_0)/(K_{\mathrm{ueff}}V)$, namely K_β, from $\phi = 180$ deg to 135 deg is relatively small, since the $|H_{\mathrm{w}}|$ value of 10 kOe is relatively small against the H_{keff} value of 67 kOe. Therefore, the increase of h from $\phi = 180$ deg to 135 deg is small.

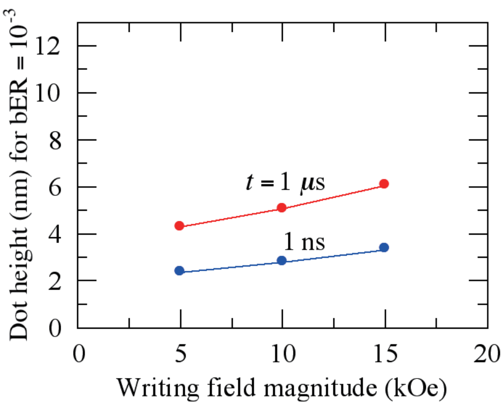

Fig. 9 Dot height h to achieve a bER of 10^{-3} as a function of writing field magnitude $|H_{\mathrm{w}}|$ after AT writing.

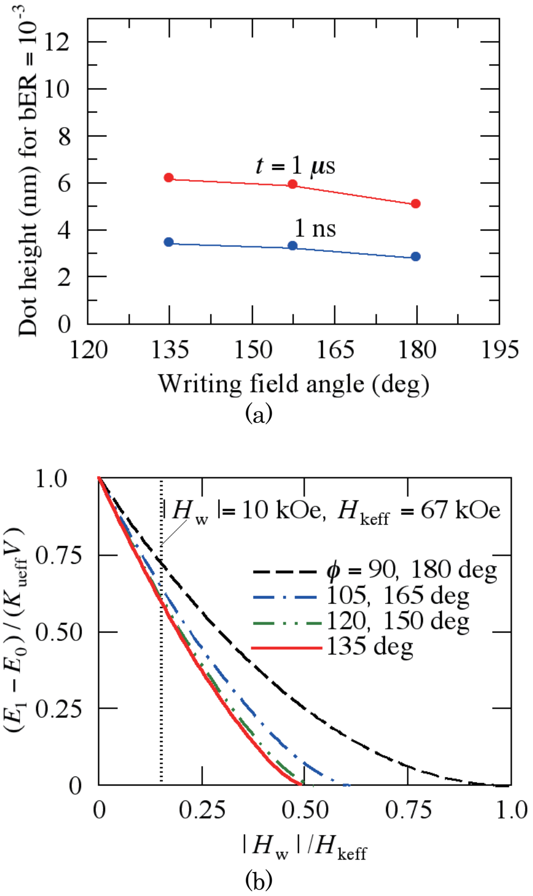

Fig. 10 (a) Dot height h to achieve a bER of 10^{-3} as a function of writing field angle ϕ after AT writing and (b) energy barrier $(E_1 - E_0)/(K_{\mathrm{ueff}}V)$ as a function of the writing field magnitude $|H_{\mathrm{w}}|/H_{\mathrm{keff}}$ for various ϕ values.

4. Conclusions

We discussed the influence of the design parameters on ATI in 4 Tbpsi HDMR. We calculated the h value to achieve a bER of 10^{-3} after AT writing as a function of the design parameters.

(1) Mean Curie temperature T_{cm}

The h value must be increased strongly as the T_{cm} value decreases, since T_{cm} and thermal gradient are closely related.

(2) Standard deviation $\sigma_{\mathrm{Tc}}/T_{\mathrm{cm}}$

In addition to the increased probability of a low T_{c} dot appearing, the adjacent track temperature is related to the $\sigma_{\mathrm{Tc}}/T_{\mathrm{cm}}$ value via the writing temperature.

(3) Anisotropy constant ratio $K_{\mathrm{u}}/K_{\mathrm{bulk}}$

The h value must be more than doubled for a decrease in the $K_{\mathrm{u}}/K_{\mathrm{bulk}}$ value from 0.8 to 0.4.

(4) Standard deviation $\sigma_{\mathrm{D}}/D_{\mathrm{m}}$

The probability of a small dot appearing increases as the $\sigma_{\mathrm{D}}/D_{\mathrm{m}}$ value increases.

(5) Gilbert damping constant α

The α value has little effect on 10 years of archiving but has an effect on ATI.

(6) Writing field magnitude $|H_{\mathrm{w}}|$

The h value must be increased as the $|H_w|$ value increases.

(7) Writing field angle ϕ

Since the $|H_w|$ value of 10 kOe is relatively small, the increase in the h value is relatively small when the ϕ value changes from 180 to 135 deg.

Acknowledgement We acknowledge the support of the Advanced Storage Research Consortium (ASRC), Japan.

References

1) S. H. Charap, P. -L. Lu, and Y. He: *IEEE Trans. Magn.*, **33**, 978 (1997).
2) T. Kobayashi, Y. Nakatani, and Y. Fujiwara: *J. Magn. Soc. Jpn.*, **47**, 1 (2023).
3) T. Kobayashi, Y. Isowaki, and Y. Fujiwara: *J. Magn. Soc. Jpn.*, **39**, 8 (2015).
4) F. Akagi, M. Mukoh, M. Mochizuki, J. Ushiyama, T. Matsumoto, and H. Miyamoto: *J. Magn. Magn. Mater.*, **324**, 309 (2012).
5) T. Kobayashi and Y. Nakatani: *J. Magn. Soc. Jpn.*, **47**, 57 (2023).
6) M. Mansuripur and M. F. Ruane: *IEEE Trans. Magn.*, **MAG-22**, 33 (1986).
7) J. -U. Thiele, K. R. Coffey, M. F. Toney, J. A. Hedstrom, and A. J. Kellock: *J. Appl. Phys.*, **91**, 6595 (2002).
8) E. D. Boerner and H. N. Bertram: *IEEE Trans. Magn.*, **34**, 1678 (1998).
9) T. Kobayashi and I. Tagawa: *J. Magn. Soc. Jpn.*, **47**, 128 (2023).
10) H. Pfeiffer: *Phys. Status Solidi* (a), **118**, 295 (1990).

Received Oct. 28, 2023; Revised Jan. 24, 2024; Accepted Feb. 26, 2024

INDEX

J. Magn. Soc. Jpn., **48**, 47-52 (2024) <Paper>

Viscosity Effects on Relaxation Time Differences of Magnetic Nanoparticles

M. Washino, K. Nomura, T. Matsuda, S. Seino*, T. Nakagawa*, T. Kiwa**, A. Tanaka***, and T. Sakane***
Mitsubishi Electric Corp., *8 -1 -1 Tsukaguchi-Honmachi, Amagasaki, Hyogo 661 -8661, Japan*
*Osaka Univ., *2 -1 Yamadaoka, Suita, Osaka 565 -0871, Japan*
**Okayama Univ., *1 -1 -1 Tsushimanaka, Okayama Kita-ku, Okayama 700 -0082, Japan*
***Kobe Pharmaceutical Univ., *4 -19 -1 Motoyamakitamachi, Higashinada-ku, Kobe-shi, Hyogo, 658 -8558, Japan*

Increased fluid viscosity in vivo is associated with diseases such as hypertension, atherosclerosis, and cancer. Fortunately, viscosity distribution enables pathological diagnosis. Magnetic-particle imaging (MPI), which detects the high-frequency magnetic field response of magnetic nanoparticles (MNPs) for obtaining highly sensitive images, can be applied to viscosity mapping to obtain a solvent viscosity distribution based on the relaxation time of MNPs. In this study, we assessed the relaxation time differences of MNPs in media with varying viscosities, detected as phase differences in the signal using an MPI system. The differences, which increases with more viscosity, differ depending on the particle size and the magnetic properties of the magnetic nanoparticles.

Keywords: magnetic particle imaging, magnetic nanoparticles, Brownian relaxation, Neel relaxation, viscosity mapping

1. Introduction

Magnetic-particle imaging (MPI), which detects and visualizes the nonlinear response of magnetic nanoparticles (MNPs) to an external magnetic field, is attracting attention as a new medical imaging technique[1]. Recently, the dynamic properties of MNPs, such as their alternating current (AC) magnetization characteristics in solution, have been studied intensively. For example, the magnetic relaxation time generally changes when MNPs are present in media with different viscosities[3]. In vivo fluid viscosity mapping has been proposed as an MPI application that utilizes the viscosity effect on the magnetic relaxation behavior of MNPs[3-4]. Elevated fluid viscosity levels in vivo are closely associated with several diseases, including hypertension[5], atherosclerosis[6], and cancer[7], and the possibility of viscosity mapping using MPI is highly anticipated for the diagnosis of such pathological conditions.

We developed an MPI system capable of detecting differences in the magnetic properties and relaxation times of MNPs in different media as signal-phase differences[8]. Arbitrary MNPs can be distinguished based on phase differences and only image arbitrary MNPs via signal processing.

In this study, we evaluated the relaxation time differences among three distinct MNPs in media with different viscosities, detecting it as a phase difference in the signal through an MPI system. We detail the results of our investigation on the changes in the magnetic relaxation times of MNPs owing to viscosity effects and their influence on signal intensity.

Corresponding author: M. Washino
(e-mail: Washino.Masaomi@ap.MitsubishiElectric.co.jp).

2. Theory

When an alternating magnetic field is applied to magnetic nanoparticles, two relaxation mechanisms exist for the magnetic moment: Brownian and Néel. In the Brown relaxation mechanism, the magnetic moment relaxes owing to the particle's rotation. Therefore, in a highly viscous medium, the rotation of MNPs is restricted, lengthening the relaxation time. By contrast, in the Néel relaxation mechanism, the relaxation time is independent of the medium's viscosity because of the magnetic moment's rotation in the particle. Magnetic relaxation time τ_E of the MNP can be expressed as Eq. (3) using Brown relaxation time τ_B and Néel relaxation time τ_N[9]:

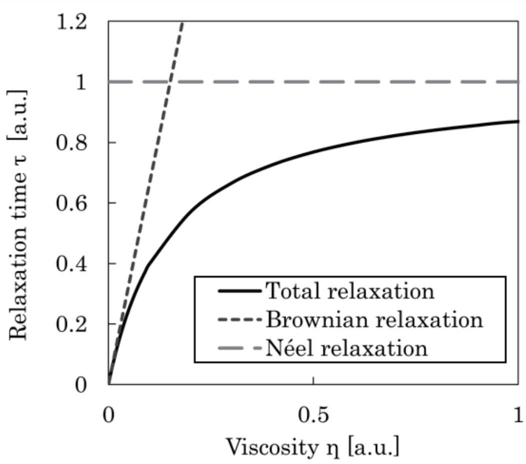

Fig. 1 Relaxation times numerically calculated as function of viscosity

$$\tau_{\mathrm{B}} = \frac{\pi\eta d_{\mathrm{H}}^{3}}{2k_{\mathrm{B}}T} \tag{1}$$

$$\tau_{\mathrm{N}} = \tau_{0} exp\left(\frac{\pi K d_{\mathrm{c}}^{3}}{6k_{\mathrm{B}}T}\right) \tag{2}$$

$$\tau_{\mathrm{E}} = \frac{\tau_{\mathrm{N}}\tau_{\mathrm{B}}}{\tau_{\mathrm{N}} + \tau_{\mathrm{B}}} \tag{3}$$

where d_{c} denotes the core particle size of the MNPs, d_{H} denotes the hydrodynamic particle size of MNPs, η denotes the viscosity of the medium, K denotes the magnetic anisotropy energy constant, k_{B} denotes Boltzmann's constant, and T denotes absolute temperature. As observed from the three equations above, the magnetic relaxation time varies for different MNP particle sizes, magnetic properties, and medium viscosities. It increases with more viscosity based on the Brown relaxation mechanism and converges to the Néel relaxation time as the viscosity increases (Fig. 1).

3. Material and Methods

3.1 Field-free line MPI System

Fig. 2 present an overview and a diagram of our developed MPI system[8]. It employs a field-free line (FFL) method, which forms a zero-field region on a line by arranging opposing magnets that combine a U-shaped iron core with permanent magnets. The FFL method has a wider signal acquisition area and a higher detected signal intensity than the field-free point (FFP) method, which forms a point-shaped zero-field region. Therefore, the FFL method is suitable for acquiring signals from objects with a small number of magnetic nanoparticles[10]. In this system, the sample is simultaneously translated using a coil system that integrates the excitation and receiver coils, and the sample is rotated and scanned to acquire projection data and reconstruct a cross-sectional image. The gradient field strength can be continuously varied from 1 to 4 T/m by changing the distance between the opposing magnets. In this study, the value was set to 1.5 T/m. The AC magnetic field generated by the excitation coil had an amplitude of approximately 30 $\mathrm{mT_{p\text{-}p}}$ (30 $\mathrm{A_{p\text{-}p}}$) at 500 Hz. A main feature of this system is that the phase difference of the measured MPI signal can be calculated by referring to the energizing current of the excitation coil using a lock-in amplifier. Since the phase difference information is determined by the time constant of the measurement device and the relaxation time of the magnetic nanoparticles, phase differences can be used to discriminate from noise and evaluate the relaxation time change of the MNPs. However, phase measurement with a lock-in amplifier is affected by the signal propagation characteristics of the measurement system in addition to the signal response from the MNPs. Therefore, it is difficult to only evaluate the phase change caused by the relaxation time of the MNP as an absolute value[11]. However, if the signals of different MNPs are compared without changing the configuration of the measurement system, the phase difference caused by only the relaxation time of the MNP can be extracted from the phase change, enabling a relative evaluation based on the phase difference and the detection frequency. For example, relaxation time difference $\Delta\tau_{\mathrm{E}}$ between samples 1 and 2 can be calculated using Eq. (4) [8]:

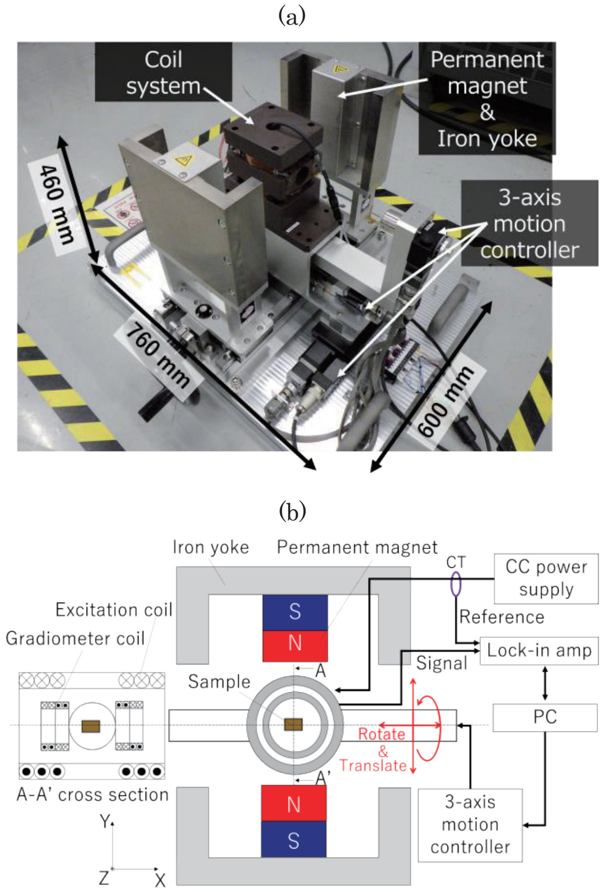

Fig. 2 MPI system using FFL generated by permanent magnet: (a) its appearance and (b) its diagram

$$\Delta\tau_{\mathrm{E}} = -\frac{\theta_1 - \theta_2}{(360\omega_{\mathrm{r}}/2\pi)} = -\frac{\Delta\theta}{360 f_{\mathrm{r}}} \tag{4}$$

where θ_1 and θ_2 denote the signal phase of each sample and f_{r} denotes the frequency of the harmonic. Since the phase difference measured here is expressed in terms of a 360° period, a relaxation time difference exceeding one period cannot be properly evaluated. The system uses a low AC field frequency of approximately 1 kHz. For example, when an AC field frequency of 500 Hz is used, one period of the third harmonic is more than 600 μsec, which is sufficiently longer than the relaxation time of the magnetic particles, enabling the evaluation of relaxation time differences due to phase differences.

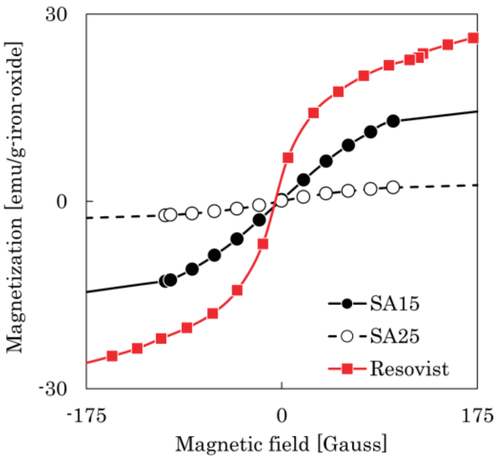

Fig. 3 Enlarged view of numerically assumed M-H curve for MPI measurement range.

3.2 Measurement samples

We prepared three types of magnetic nanoparticles to investigate the effects of particle size and the magnetic properties on the magnetic relaxation time. One was Resovist (commercially distributed by FUJIFILM RI Pharma, Japan) and the other two were MNPs with core particle sizes of 25 nm (SA25) and 15 nm (SA15) (Sigma-Aldrich). The hydrodynamic particle sizes of SA25 and SA15 were 35.9 and 62.5 nm by dynamic light scattering (DLS)[8]. The core particle size and the hydrodynamic particle size of Resovist were obtained from T. Yoshida et al.[9] Fig. 3 shows the DC susceptibility characteristics of each MNP[8]. In the range of AC field strengths used in this study, the DC magnetization of Resovist is the largest; that of SA25 is the smallest.

Subsequently, MNP samples with different viscosities were prepared. Viscosity was adjusted by adding a thickening agent to three different MNP solutions (900 μL each). Hydroxypropyl cellulose (HPC) was used as a thickener in amounts (sealed in a 460 μL vial) that varied in four ways: 0 (no addition), 1, 2, and 3% of the solution volume. Fig. 4 shows the 12 samples. Fig. 5 shows the results of the viscosity measurements of the 12 samples. The viscosity increased with the amount of additional HPC, and samples with different viscosities were obtained in the range of 1~500 mPa-s.

4. Results and Discussion

4.1 Viscosity dependence of relaxation time differences

The magnetic signals were acquired by scanning the prepared magnetic nanoparticle samples along the x-axis of the MPI system. A single X-axis scan takes only 5 min. Fig. 6 shows the Lissajous curve of the third-harmonic signal in the Resovist sample series at an AC magnetic field frequency of 500 Hz. The phase angle was adjusted such that the vertical axis (imaginary part) coincided with the Lissajous curve for the case of 0%, which

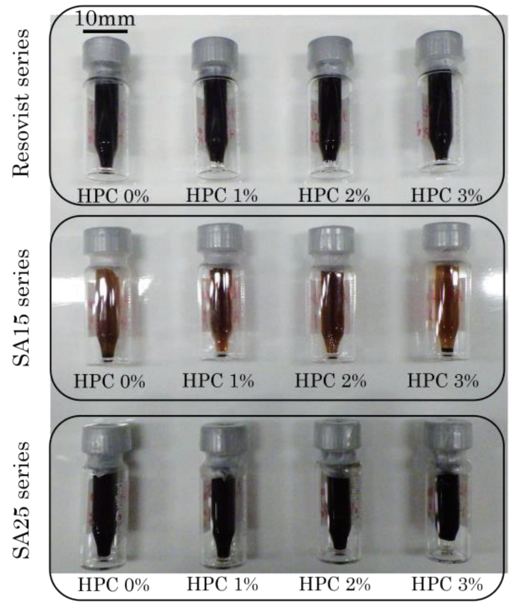

Fig. 4 MNP encapsulated cylinder samples (volume:460 μL)

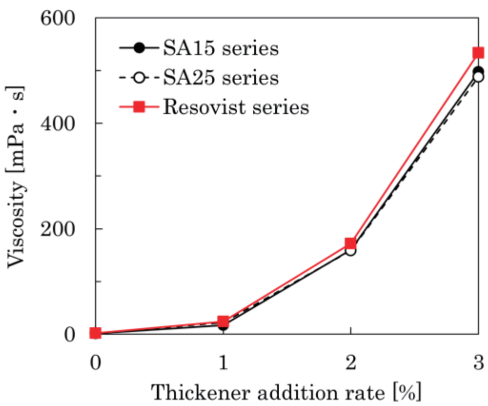

Fig. 5 Sample viscosity versus thickener addition rate

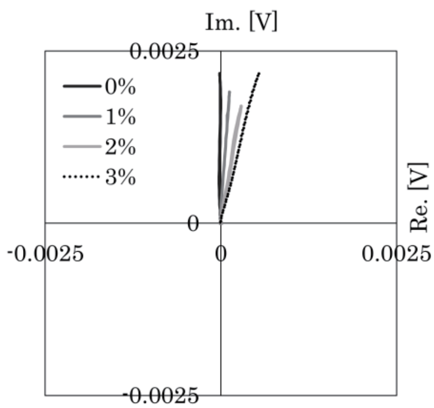

Fig. 6 Lissajous curve of 3rd harmonic signal of Resovist sample series at 500 Hz

coincided with the Lissajous curve for the case of 0% thickener addition to facilitate comparison of the differences in the phase angle. We confirmed that it changed based on the amount of added thickener (difference in viscosity). Third-harmonic signals were also obtained for the SA25 and SA15 sample series at an AC field frequency of 500 Hz. The phase angle changed based on the amount of added thickener (difference in viscosity).

Fig. 7 shows the calculated phase differences for each amount of thickener added to each sample using the phase of the Lissajous curve when the amount of thickener added as a reference is 0%. Fig. 8 shows the calculated relaxation time difference from the phase difference shown in Fig. 7 using Eq. (4). The relaxation time differences increased with viscosity, regardless of the type of magnetic nanoparticles. In the low viscosity range (tens of mPa-s), all the MNP samples show a large increase in the relaxation time difference as the viscosity increases. As the viscosity increased further, the difference in the relaxation time saturated to a constant value. This result indicates that in a low viscosity range of several tens of mPa-s, the viscosity-dependent Brown relaxation time is dominant for all MNPs, but in the high viscosity range, the viscosity-independent Néel relaxation time tends to converge. The SA15 sample series had the smallest relaxation time difference among the three MNP sample series; SA15 had a shorter Brownian relaxation time owing to its smaller hydrodynamic particle size than the other two MNPs. SA15 also had a shorter Néel relaxation time owing to its smaller core particle size than the other two MNPs. Therefore, because the Néel relaxation time was dominant for SA15 in the viscosity range measured in this study, the viscosity dependence of the relaxation time difference is small, and the relaxation time difference is the smallest among the three MNPs. In contrast, the Resovist sample series exhibits the largest relaxation time difference among the three MNP samples. Since Resovist and SA25 have comparable core and hydrodynamic particle sizes, we infer that the contrast was caused by differences in their saturation magnetization. Resovist exhibits a higher saturation magnetization than SA25 (Fig. 3). Consequently, the relaxation time is prolonged, resulting in a correspondingly larger relaxation time difference. These results suggest that among the three MNPs, Resovist, which has the largest relaxation time difference for different viscosities, is the most suitable for viscosity mapping in a viscosity range of 1~500 mPa-s measured in this study.

4.2 Frequency of AC magnetic field dependence of relaxation time difference and signal intensity

To investigate the effect of AC field frequency on the relaxation time difference, third-harmonic signals were obtained at AC field frequencies of 500, 800, and 1200 Hz.

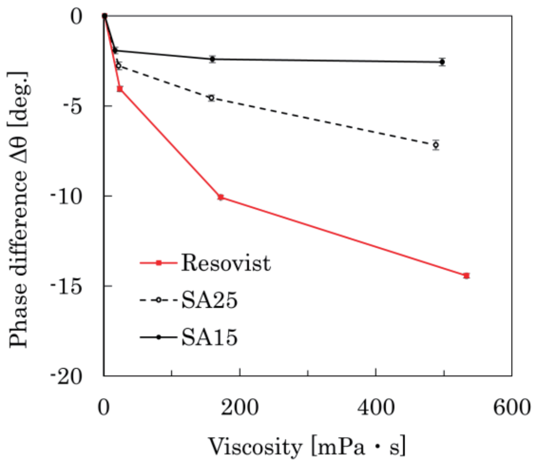

Fig. 7 Phase differences calculated for various thickener addition levels, using 0% thickener as reference

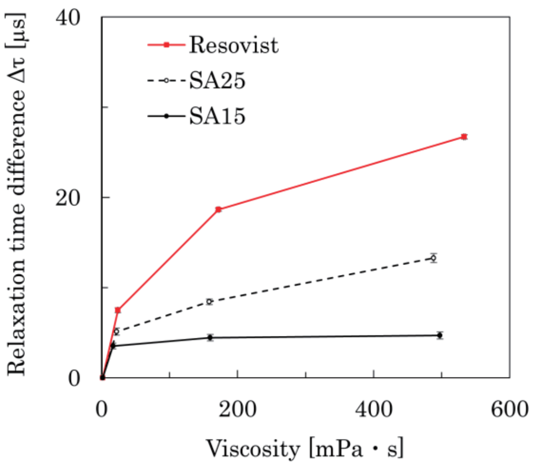

Fig. 8 Relaxation time differences calculated from phase differences at various levels of thickener addition, with 0% thickener addition as reference

Fig. 9 shows the viscosity dependence of the relaxation time differences for each magnetic nanoparticle as the AC field frequency is varied. Figs. 9(a), (b), and (c), which show the measurement results of the Resovist, SA25, and SA15 sample series, respectively, indicate that the relaxation time difference tends to decrease as the AC field frequency increases, regardless of the MNP type. This result can be attributed to the fact that the magnetic relaxation behavior of the MNPs cannot follow an increase in the AC field frequency. Therefore, the lower the AC magnetic field frequency, the larger the relaxation time difference, which is suitable for viscosity mapping.

The effects of AC field frequency and viscosity on the signal intensity were also investigated. Figs. 10(a), (b), and (c) show the results for the Resovist, SA25, and SA15

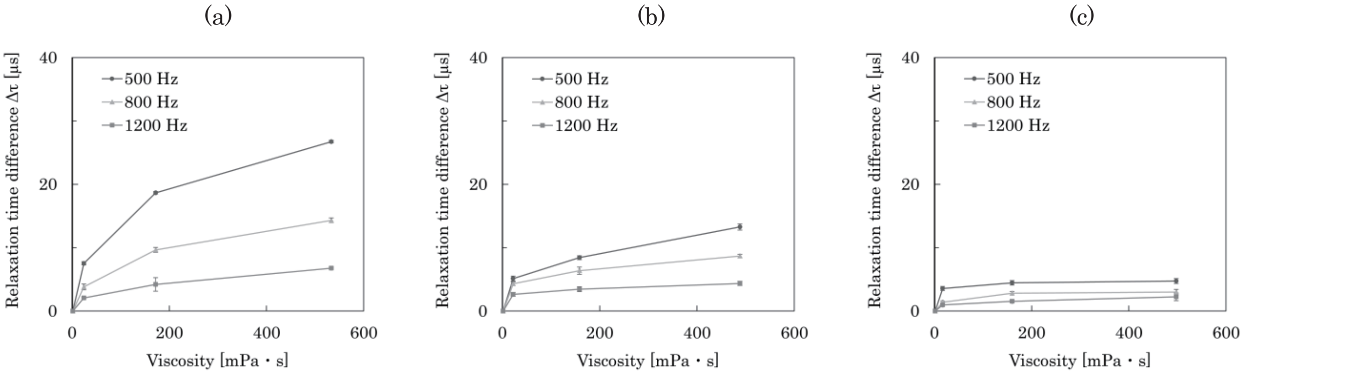

Fig. 9 AC field frequency dependence of relaxation time differences as function of viscosity: (a) Resovist sample series, (b) SA25 sample series, and (c) SA15 sample series.

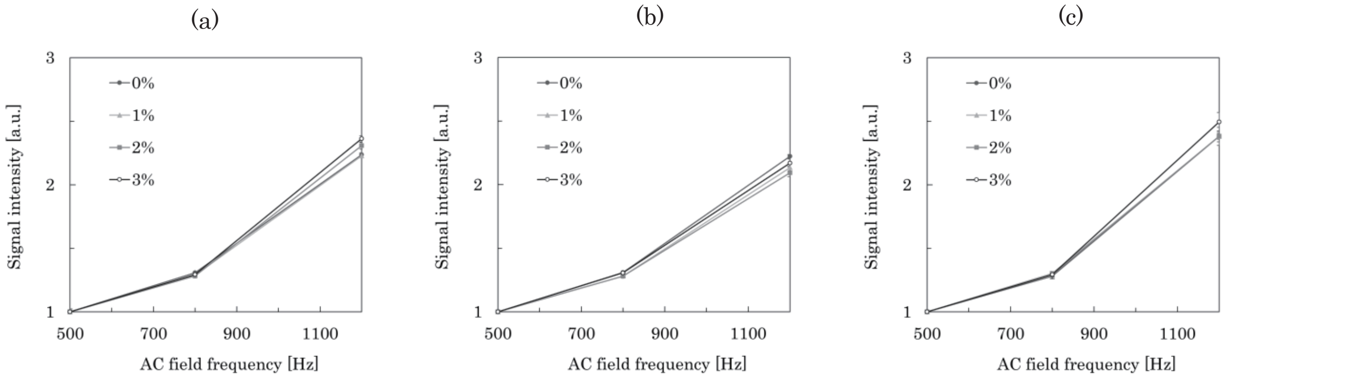

Fig. 10 Viscosity dependence of signal intensity as function of AC field frequency, using signal strength at 500 Hz as reference: (a) Resovist sample series, (b) SA25 sample series, (c) and SA15 sample series.

sample series. For all the MNP samples, the signal intensity increases approximately linearly with the AC field frequency. The ratio of the increase in the signal intensity to the AC field frequency is constant, regardless of the amount of thickener added (viscosity). Since the signal intensity increases linearly with the AC field frequency, regardless of the viscosity, using a high AC field frequency is preferable for the viscosity mapping of objects with small magnetic signals.

5. Conclusion

In this study, we prepared three types of MNPs with different particle sizes and magnetic properties and investigated the effect of viscosity on the magnetic relaxation times of the MNPs and the signal intensities. Regardless of the type of MNPs, we confirmed that the relaxation time difference increased with the viscosity in the viscosity range of 1~500 mPa-s. Among the three MNPs, Resovist exhibited the largest change in the relaxation time difference as the viscosity increased. Moreover, we confirmed that the relaxation time difference tends to decrease as the AC field frequency increases, regardless of the MNP type; the signal intensity increases. These results indicate that our MPI system can measure changes in the magnetic relaxation time owing to viscosity effects and suggests its potential application to viscosity mapping. For viscosity mapping, MNPs must be selected with a dominant Brown relaxation time in the viscosity range of interest, and a large relaxation time difference is desirable for accurately discriminating the viscosity. Although the relaxation time difference increases when a low AC field frequency is used, it causes a decrease in the signal strength. To achieve a significant difference in relaxation time and an enhanced signal strength (yielding a high signal-to-noise ratio), the choice of AC magnetic field frequency should be carefully considered based on the dimensions and viscosity of the magnetization under examination. In the future, we intend to conduct specific viscosity mapping to evaluate the spatial resolution of this mapping technique.

Acknowledgments This research was supported by the Advanced Measurement and Analysis Technology and Instrument Development Program of the Japan Agency for Medical Research and Development (project number JP22 hm0102073).

References

1) B. Gleich and J. Weizenecker: *Nature*, **435**, 1214 (2005).
2) K. Jinno, T. Kiwa et al.: *AIP Adv.*, **9**, 125317 (2019).
3) M. Utkur, Y. Muslu, and U. Saritas: *Phys. Med. Biol.*, **62**, 3422 (2017).
4) S. Draack and N. Niklas: *J. Phys. Chem. C,* **123**, 6787 (2019).
5) G. Tibblin, S. E. Bergentz et al.: *Am. Heart J.*, **72**, 165 (1966).
6) G. D. Lowe, M. M. Drummond et.al: *BMJ*, **280**, 673 (1980).
7) M. F. Guyer and P. E. Claus: *Cancer Res.*, **2**, 16 (1942).
8) K. Nomura, M. Washino et al.: *IEEE Magn. Lett.*, **14**, 8100105 (2023).
9) T. Yoshida, T. Nakamura, O. Higashi, and K. Enpuku: Jpn. *J. Appl. Phys.*, **57**, 080302 (2018).
10) J. Weizenecker, B. Gleich, and J. Borgert: *J. Phys. D, Appl. Phys.*, **41**, 105009 (2008).
11) K. Umeo: *Rev. High Press. Sci. Technol.*, **25**, 283 (2015).

Received Oct. 13, 2023; Revised Jan. 16, 2024; Accepted Feb. 26, 2024

INDEX

J. Magn. Soc. Jpn., **48**, 53-59 (2024)

<Paper>

Design method of surface receive coil with high SNR for various field intensities in MRI

Masaharu Takahashi*, Motofumi Fushimi**, Shin Yabukami*, ***,

Masaki Sekino**, and Akihiro Kuwahata*,***

* Graduate School of Engineering, Tohoku Univ., *6-6-05 Aramaki-aza-Aoba, Aoba-ku, Sendai 980-8579, Japan*

** Graduate School of Engineering, The University of Tokyo, *7-3-1 Hongo, Bunkyo-ku, Tokyo 113-8656, Japan*

*** Graduate School of Biomedical Engineering, Tohoku Univ., *6-6-05 Aramaki-aza-Aoba, Aoba-ku, Sendai 980-8579, Japan*

Magnetic resonance imaging (MRI) is a noninvasive medical imaging technology with a high spatial resolution. We aim to design a single-channel radiofrequency receive coil with an optimized signal-to-noise ratio (SNR) for various field intensities in MRI. We propose a method that maximizes the SNR through surface current optimization using the target field method. The proposed method can design a dedicated coil shape by solving an objective function with terms related to the signal, coil resistance noise and sample resistance noise. We found coil shapes for a rat kidney model in the case of static magnetic field intensity $|\boldsymbol{B}_0| = 7$ T, 0.3 T and 6.5 mT as an example. Our method will enable the design of single channel receive coil for preclinical applications of small animals.

Keywords: magnetic resonance imaging, signal-to-noise ratio, radiofrequency coil, receive coil, target field method

1. Introduction

The fundamental issue in magnetic resonance imaging (MRI) is improving the signal-to-noise ratio (SNR) of the received signal to get images with high spatial resolution [1]. For example, the measurement of glomeruli (spherical structures with diameters ranging from 10 – 100 μm) to diagnose kidney disease. In imaging with voxel sizes around 10 μm, Clinical MRI (scan time ≤ 60 min.) has insufficient image SNR, making it impossible to measure the number of glomeruli [2].

The main magnet generates a static magnetic field ($\boldsymbol{B}_0$), inducing the precession of spins at a frequency of $f_0 = \gamma|\boldsymbol{B}_0|$ (γ is the gyromagnetic ratio of proton) along its direction. The transmit coil produces a radiofrequency (RF) magnetic field (B_1^+) rotating at a frequency of f_0, causing the spin vector to deviate from the direction of $\boldsymbol{B}_0$. Once B_1^+ is deactivated, the magnetization returns to its initial state with precession, inducing a voltage in the RF receive coil.

Spatial resolution is the minimum voxel size capable of distinguishing adjacent pixels [3]. Decreasing the voxel size results in a lower SNR for the image. This is because the received signal from a target point r_0 decrease with the voxel size V according to the following equation [4]:

$$Signal(r_0) = \omega_0 V M_0 |B_1^-(r_0)|, \tag{1}$$

where $\omega_0 = 2\pi f_0$, M_0 ($\propto |\boldsymbol{B}_0|$) is the magnetization, and $|B_1^-|$ is the sensitivity distribution of the receive coil. Decreasing the voxel size is achieved by reducing the bandwidth of transmit and receive coils and increasing the gradients of $\boldsymbol{B}_0$. To obtain sufficient SNR in images for distinguishing adjacent voxels (enhancing spatial resolution) despite reducing the pixel size, an improvement in the SNR of received signals is necessary. Enhancing the SNR of received signals can be achieved by increasing $\boldsymbol{B}_0$ ($\omega_0 \propto |\boldsymbol{B}_0|$, $M_0 \propto |\boldsymbol{B}_0|$, $Signal \propto |\boldsymbol{B}_0|^2$), increasing the number of imaging sequences, and using receive coils with high SNR [5),6)]. Improving the SNR of receive coils is effective to decrease installation effort of higher $\boldsymbol{B}_0$ scanner and to make scan time shorter.

For $\boldsymbol{B}_0$ along the z-axis, B_1^- is expressed as the following equation[7)]:

$$B_1^- = \frac{\left(B_{1,\mathrm{x}} - iB_{1,\mathrm{y}}\right)^*}{2}, \tag{2}$$

where $B_{1,\mathrm{x}}$ and $B_{1,\mathrm{y}}$ are the respective x- and y-components of the RF magnetic field ($\boldsymbol{B}_1$) produced by the coil with unit current, i is the imaginary unit, and the asterisk denotes a complex conjugate. The noise is evaluated using the following equation [4)]:

$$Noise = \sqrt{4kTR\Delta F}, \tag{3}$$

where k is the Boltzmann constant, T denotes the effective temperature of a system, R is the equivalent resistance, and ΔF is the frequency bandwidth of the RF coil. As k, T and ΔF are not determined only by the coil shape, we simplify the noise as $\sqrt{R}$. In MRI system, R originates from the coil resistance R_{coil} and sample resistance R_{sample} as the following: $Noise \propto \sqrt{R} = \sqrt{R_{\mathrm{coil}} + R_{\mathrm{sample}}}$. R_{coil} and R_{sample} are expressed as the following equations [8)–11)]:

$$R_{\mathrm{coil}} = \frac{l}{\varphi}\sqrt{\frac{\rho\mu_0 f_0}{\pi}}, \tag{4}$$

$$R_{\mathrm{sample}} = \sigma\int \boldsymbol{E}\cdot\boldsymbol{E}\,dv = \sigma{\omega_0}^2\int \boldsymbol{A}\cdot\boldsymbol{A}\,dv, \tag{5}$$

where ρ is the resistivity of the coil's windings, l is the total length of the windings, φ is the diameter of the winding, μ_0 is the magnetic permeability of the free space, $\boldsymbol{E}$ is the electric field, $\boldsymbol{A}$ is the magnetic vector

Corresponding author: A. Kuwahata (e-mail: akihiro.kuwahata.b1@tohoku.ac.jp).

potential, v is the volume of the sample, and σ is the conductivity of the sample. For eq. (5), the units of $\boldsymbol{E}$, $\boldsymbol{A}$ and R_{sample} are (V/m)/A, (Wb/m)/A and W/A^2 = Ω, respectively, because the values of $\boldsymbol{E}$ and $\boldsymbol{A}$ are calculated based on the unit current flowing the coil. Please refer to details in the references [4), 9)]. Thus, we define the simplified SNR by the following equation:

$$SNR(\boldsymbol{r_0}) = \frac{|\boldsymbol{B}_0|^2|B_1^-(\boldsymbol{r_0})|}{\sqrt{R_{\text{coil}} + R_{\text{sample}}}}. \quad (6)$$

An ultra-high field scanner (for $|\boldsymbol{B}_0| \geq$ 7 T, $f_0 \geq$ 298 MHz) is often used to enhance the SNR in preclinical research on organs such as kidney [12)]. Previously, we had focused on the numerical design of a single channel receive coil for rat kidney imaging at 7 T [10)]. Most conventional coils dedicated to small animal organ were designed using the existing knowledge of the traditional forward problem, which does not always enable an optimized SNR [2),13)–15)]. The target field method is a well-known numerical method in the optimization of electromagnetic coils based on the inverse problem approach, presented by Turner [16)] for a cylindrical MRI gradient coil. This method calculates the magnetic field using direct current (DC) analysis for the defined basis surface currents and find surface currents to achieve the minimum error between the target field and produced field. Several research applied the method to the design of RF coils [17)–21)]. However, some of them aimed to improve the homogeneity of the magnetic field distribution, not SNR [17)–19)]. Others aimed to maximize SNR but the definition of the noise is not clear [20),21)]. Therefore, we previously proposed a method to maximize the SNR through the surface current optimization using target field method based on the inverse problem approach [10)].

For MRI applications, DC inverse problem approach lacks the calculation of the phase difference of current, eddy current, and displacement current, in contrast to forward problem approach based on alternative current (AC) using electromagnetic simulation such as the finite-difference time-domain (FDTD) method [13)–15)], the finite-element method [22)], and the method of moments [23)]. However, to formulate the relation between RF current and RF field at target region for inverse problem analysis is computationally too complex, suggesting the uncertainty of the solution. We had confirmed that our previous proposed coil achieved an SNR of 1.05-fold compared with the conventional coil. Although the relative SNR of proposed coil to the conventional coil calculated by the DC analysis was 1.13 and the error of relative SNR between DC and AC analysis of 8 % exists, we verified a coil that exhibits higher SNR in DC analysis can yield higher SNR in AC analysis in the range of the target object size (Depth from coil surface: 5 – 15 mm), frequency (298 MHz) and electrical parameters (Electrical conductivity σ = 0.55 (S/m), Relative permittivity: ε_r = 51.95), suggesting that the method is effective for design of RF receive coil for 7 T MRI.

However, in the case of standard clinical MRI devices ($|B_0|$ = 1.5 T and 3 T in the superconducting magnets and $|B_0|$ =0.2 – 0.5 T in the permanent magnets [24),25)]), R_{coil} is dominant compared to R_{sample} due to the lower frequency of f_0. Additionally, there is significant ongoing exploration into ultra-low magnetic fields ($|B_0| <$ 0.2 T) [26)]. Shen *et al.* [27)] had proposed a method to maximize the SNR through the coil winding combination optimization using target field method for human brain at 6.5 mT. This method calculates B_1^- for the defined windings and find a winding combination to achieve the balance of the minimum error between the target field and produced field (i.e. higher $Ave.(|B_1^-(ROI)|)$) and lower length of windings (i.e. lower R_{coil}). The drawback of this method is limited degree of obtained coil shape's freedom.

The purpose of this study is to design a single-channel RF receive coil with an optimized SNR for various field intensities in MRI. We propose an expanded method of our previous study [10)] to maximize the SNR through the surface current optimization using target field method. In the objective function, we clarify terms related to $Ave.(|B_1^-(ROI)|)$, R_{sample} and R_{coil}, and explore the balance of terms related to R_{sample} and R_{coil}. We design coil shapes for a rat kidney model in the case of $|\boldsymbol{B}_0| = 7$ T, 0.3 T and 6.5 mT as example.

2. Methods

We design the coil shape by defining the magnetic field distribution for the target region. The magnetic field produced by a current in the free space is described by the following equation:

$$\boldsymbol{B} = \frac{\mu_0 j}{4\pi} \oint_P \frac{\boldsymbol{r}-\boldsymbol{r_0}}{|\boldsymbol{r}-\boldsymbol{r}_0|^3} \times d\boldsymbol{l} = \boldsymbol{C}'\boldsymbol{J}, \quad (7)$$

where j is a current flowing on a closed path (P), $d\boldsymbol{l}$ is the unit vector along P, $\boldsymbol{r}$ is the position vector on P, $\boldsymbol{r}_0$ is the position vector on a target point, $\boldsymbol{C}'$ is the field coupling matrix of the coil surface to the target points, and $\boldsymbol{J}$ is the surface current vector. Using the stream function $\psi = \boldsymbol{s}^T\hat{\boldsymbol{h}}$, which is defined as the following equation: $\boldsymbol{J} = \nabla\psi \times \hat{\boldsymbol{n}}$, where $\hat{\boldsymbol{n}}$ is the normal vector to the surface, and $\boldsymbol{s}$ is the vector of the weight of the surface harmonics vector ($\hat{\boldsymbol{h}}$), we can obtain $\boldsymbol{B} = \boldsymbol{C}\,\boldsymbol{s}$, where $\boldsymbol{C}$ is the field coupling matrix of the surface harmonics to the target points.

We used a software package: bfieldtools [28),29)] in Python 3.7 for the inverse problem analysis. In this tool, ψ is represented on a mesh-by-mesh basis of the specified surface, allowing for inverse problem analysis on any arbitrary coil surface. The analysis was divided to three processes. First, we define coil surface mesh, target points, and field distribution at target points ($\boldsymbol{B}_{\text{t}}$). $\hat{\boldsymbol{h}}$ (length: N_{h}) is defined on the coil surface. The target points are set in two regions, Region Signal (number of points: M_{signal}) and Region Noise (number of points: M_{noise}). For the field distribution in Region Signal ($\boldsymbol{B}_{\text{t, signal}}$ (shape: $M_{\text{signal}} \times 3$)), one of the components orthogonal to $\boldsymbol{B}_0$ is 1 and others are 0. For the field distribution in Region Noise ($\boldsymbol{B}_{\text{t, noise}}$ (shape: $M_{\text{noise}} \times 3$)), all components are 0. We aim to maximize $Ave(|B_1^-(ROI)|)$, which is the average of the signal in the region of interest (ROI), and to minimize R_{sample} ($\propto \int \boldsymbol{B}_1 \cdot \boldsymbol{B}_1\, dv$). We calculate $\boldsymbol{C}_{\text{signal}}$ (shape: $M_{\text{signal}} \times 3\times N_{\text{h}}$) and $\boldsymbol{C}_{\text{noise}}$ (shape: $M_{\text{noise}} \times 3\times N_{\text{h}}$) using $\hat{\boldsymbol{h}}$ and target

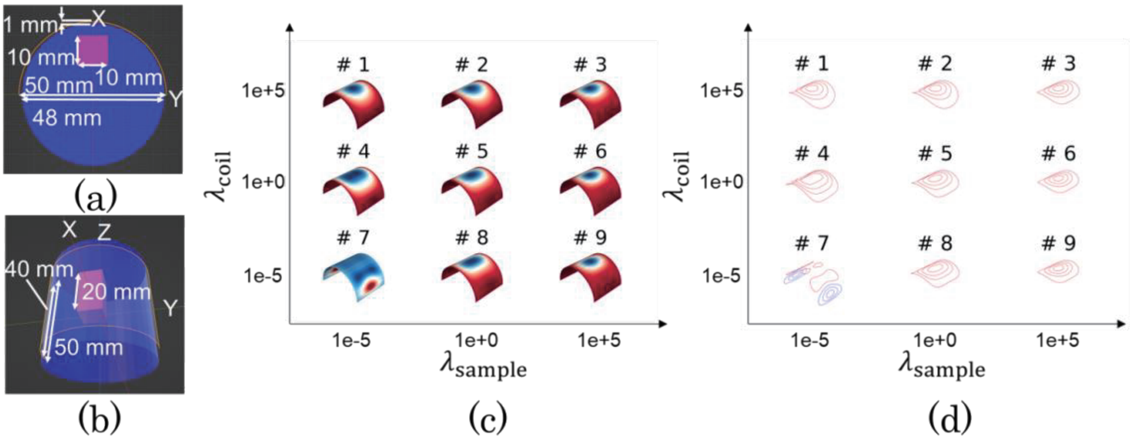

Fig. 1 Initial setup for inverse problem analysis, calculated stream functions, and coil shapes with $\lambda_{sample}, \lambda_{coil} =$ 1e-5, 1e0 and 1e5. Coil surface, Region Signal and Region Noise in xy-plane (a) and in xyz-space (b). Orange area, pink cuboid and blue cylinder corresponds to coil surface, Region Signal and Noise, respectively. (c) Calculated stream function. Color map range of stream function ψ is $[Min(\psi),\ Max(\psi)]$ and corresponds to [blue, red]. (d) Coil shapes with $N_c =$ 4. Red and blue winding are right- and left-handed loop, respectively. Size of coil surface in (c) corresponds to that in (a) and (b). The scale in (d) is same as (c).

points in Region Signal and Noise, respectively.

Second, we find $\boldsymbol{s}$ (length: N_h) that minimizes the objective function. In our previous method, we defined the objective function to increase $Ave.(|B_1^-(ROI)|)$and to decrease R_{sample}:

$$f'(\boldsymbol{s}) = |\boldsymbol{B}_t - \boldsymbol{C}\boldsymbol{s}|^2, \tag{8}$$

where the shape of $\boldsymbol{B}_t$ is $(M_{signal} + M_{noise}) \times 3$ and the shape of $\boldsymbol{C}$ is $(M_{signal} + M_{noise}) \times 3 \times N_h$. The function reaches its minimum when $\boldsymbol{s} = \boldsymbol{C}^{-1}\boldsymbol{B}_t$. In the proposed method, we define the objective function:

$$f(\boldsymbol{s}) = L_{signal} + \lambda_{sample} L_{sample} + \lambda_{coil} L_{coil}, \tag{9}$$

$$L_{signal} = \left|\boldsymbol{B}_{t,\,signal} - \boldsymbol{C}_{signal}\boldsymbol{s}\right|^2, \tag{10}$$

$$L_{sample} = \left|\boldsymbol{B}_{t,\,noise} - \boldsymbol{C}_{noise}\boldsymbol{s}\right|^2, \tag{11}$$

$$L_{coil} = \boldsymbol{s}^{\boldsymbol{T}}\boldsymbol{P}\boldsymbol{s}, \tag{12}$$

where λ_{sample} and λ_{coil} is a scalar parameter to define weight of the L_{sample} and L_{coil}, respectively, and $\boldsymbol{P}$ (shape: $N_h \times N_h$) is the ohmic energy matrix. We aim to maximize $Ave(|B_1^-(ROI)|)$, to minimize R_{sample} with proper weight, and to minimize R_{coil} with proper weight. The function reaches its minimum when

$$\boldsymbol{s} = \left(\boldsymbol{C}_{signal}{}^{\boldsymbol{T}}\boldsymbol{C}_{signal} + \lambda_{sample}\boldsymbol{C}_{noise}{}^{\boldsymbol{T}}\boldsymbol{C}_{noise} + \lambda_{coil}\boldsymbol{P}\right)^{-1} \left(\boldsymbol{C}_{signal}{}^{\boldsymbol{T}}\boldsymbol{B}_{t,\,signal} + \lambda_{sample}\boldsymbol{C}_{noise}{}^{\boldsymbol{T}}\boldsymbol{B}_{t,\,noise}\right). \tag{13}$$

Third, we determine the coil path design based on the calculated surface current as follows: $P_i = Min(\psi) + step \cdot \{i - (1/2)\}\ (i = 1,2,\dots,N_c)$, $step = \{Max(\psi) - Min(\psi)\}/N_c$, where N_c defines how finely the surface current is represented. Note that contour lines of the surface current correspond to the coil path and the polarity of $\boldsymbol{\nabla}\psi$ represents the direction of the current flowing on the coil path.

Optimal values of λ_{sample} and λ_{coil} depend on $|\boldsymbol{B}_0|$ of interest because of the characteristics of R_{sample} and R_{coil}. At this perspective, we obtain the coil shape for each calculated stream function with different λ_{sample} and λ_{coil} and evaluate the SNR of each shape to find the optimal values.

In this study, we employed homogeneous sample. Some research used anatomically accurate body model to assume an actual MR experiment [14),15),30)]. For example, Kim *et al.* [14)] conducted the simulation with FDTD using rat model to evaluate the coil for deep region imaging such as liver (Depth from coil surface: ~ 10 – 40 mm) and they include the regions such as backbone and muscle in the main part of the field of view (FOV) region. However, our target is a kidney and our main part of FOV is homogeneous and small compared to those of Kim *et al.* because the kidney is located the side of the backbone and near surface of the body (Depth from coil surface: ~ 5 – 15 mm) [2)], suggesting the acceptability to use the homogeneous model.

3. Results and Discussion

Figure 1 shows the configuration for the inverse problem analysis, the calculated stream functions and coil shapes. In Figs. 1(a) and (b), the cylinder with a diameter of 48 mm was the imaging object (as rat body) and a cuboid of 10 × 10 × 20 mm^3 located at a depth in the range of 4 – 14 mm from the surface of the body was the ROI (as rat kidney). The coil surface was half of the cylindrical side (diameter 50 mm, length 40 mm) and the location of the coil was 1 mm above the surface of the body. Region Signal of the target points was the ROI, a cuboid with dimensions of 10 × 10 × 20 mm^3 located at a depth in the range of 5 – 15 mm from the coil surface (2 mm interval, $M_{signal} =$ 396). Region Noise of the target points was a cylinder (diameter 48 mm, length 50 mm) except for Region Signal (2 mm interval, $M_{noise} =$ 11,348). The field distribution in Region Signal and Noise was $\boldsymbol{B}_{t,\,signal} = 1 \cdot \hat{\boldsymbol{x}} + 0 \cdot \hat{\boldsymbol{y}} + 0 \cdot \hat{\boldsymbol{z}}$ (a.u.) and $\boldsymbol{B}_{t,\,noise} = \boldsymbol{0}$ (a.u.), respectively. Note that the direction of $\boldsymbol{B}_0$ was z-axis.

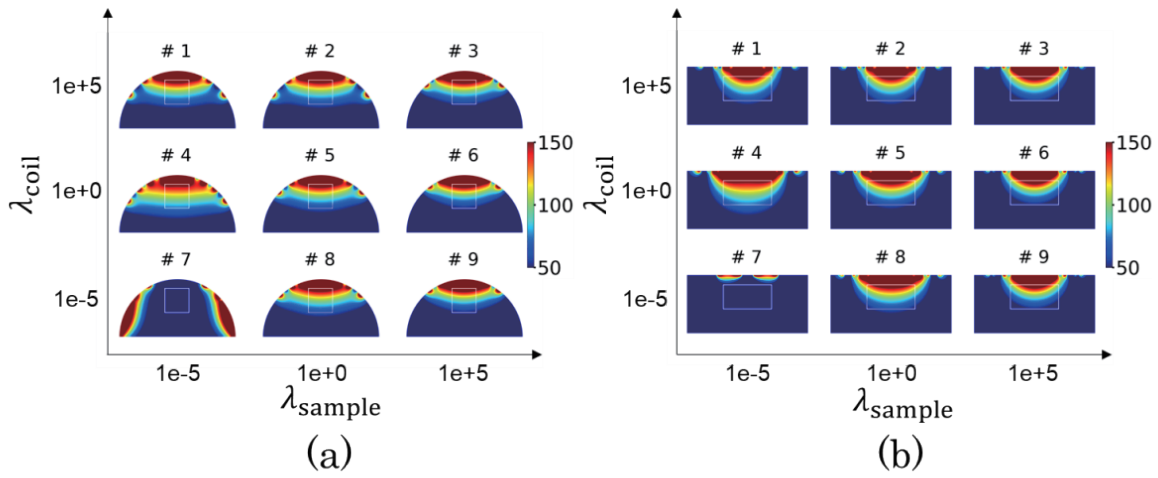

Fig. 2 $|B_1^-|$ maps of coil designed with $\lambda_{sample}, \lambda_{coil}$ = 1e-5, 1e0 and 1e5. (a) Region where x = [0, 24], y = [-24, 24], z = 0. (b) Region where x = [0, 24], y = 0, z = [-25, 25]. Unit of color map is μT. Plotted rectangular regions correspond to the region of interest (Region Signal in Fig. 1).

We calculated the stream functions with different λ_{sample} and λ_{coil} (= 1e-5, 1e-4, ..., 1e5) in the case of N_h = 20 (Fig. 1(c)). We obtained the coil shapes with N_c = 4 (Fig. 1(d)). As #1 for an example, the higher λ_{coil} yielded the shorter winding length and larger open angle (the angle formed by OQmax and OQmin, where Qmax and Qmin are points on the coil with maximum and minimum y-coordinates respectively, and O represents the origin). As #9 for an example, the higher λ_{sample} promoted the shorter winding length and smaller open angle. For #7, the shape was unique compared to others and was excluded from further discussion due to its extremely low SNR (Fig.3(d), Fig.4(d), and Fig.5(d) as mentioned later).

Figure 2 shows $|B_1^-|$ $(= (B_{1,x}{}^2 + B_{1,y}{}^2)^{1/2}$, where $B_{1,x}$ and $B_{1,y}$ are calculated using Eq. (5)) maps of coils designed with λ_{sample}, λ_{coil} = 1e-5, 1e0 and 1e5. The lower λ_{sample} and λ_{coil} enhanced $|B_1^-|$ homogeneity, resulting in the lower $Ave.(|B_1^-(ROI)|)$ because of the objective function $f(\boldsymbol{s}) \sim L_{signal} = \left|\boldsymbol{B}_{t,\,signal} - \boldsymbol{C}_{signal}\boldsymbol{s}\right|^2$. For example, the homogeneity of # 4 and # 3 was 51.7 % and 33.0 %, respectively.

Figure 3 shows the dependencies of evaluation factors, such as the signal, noise, and SNR, on λ_{sample} and λ_{coil}, in the case of $|\boldsymbol{B}_0| = 7$ T (f_0 = 298 MHz). The signal was evaluated as $|\boldsymbol{B}_0|^2 Ave.(|B_1^-(ROI)|)$. R_{coil} was calculated using Eq. (2) with the following parameters: φ = 0.5 mm, ρ = 1.68 × 10^{-8} Ω·m, and σ = 0.55 S/m [14]. R_{sample} was calculated using Eq. (5) and the magnetic vector potential as the following:

$$\boldsymbol{A} = \left\{\frac{\mu_0 j}{4\pi}\right\} \oint_P \left(\frac{d\boldsymbol{l}}{|\boldsymbol{r}-\boldsymbol{r_0}|}\right). \tag{14}$$

The signal intensity was higher at the left-center regions (λ_{coil} = 1 and $\lambda_{sample} < 1$) compared to other regions (Fig.3(a)). R_{sample} (≤ 28.4 Ω) was dominant compared to R_{coil} (≤ 1.68 Ω) (Figs. 3(b) and (c)) and the maximum SNR was 1305 and at the right-bottom corner region (λ_{coil} = 1e-5 and λ_{sample} = 1e+5) in Fig. 3(d). The corresponding coil shape was # 9 in Fig. 1(d) (winding length: 285 mm, open angle: 74.8 degrees).

Figure 4 shows the evaluation factors for $|\boldsymbol{B}_0|$ = 0.3 T. The dependence of the signal on λ_{sample} and λ_{coil} was similar to that in $|\boldsymbol{B}_0|$ = 7 T. However, the intensity was lower because it is proportional to $|\boldsymbol{B}_0|^2$ (Fig. 4(a)). R_{coil} (≤ 0.347 Ω) was dominant compared to R_{sample} (≤ 52.3 mΩ) (Figs. 4(b) and (c)). The maximum SNR was 17.9 and at the center-bottom region (λ_{coil} = 1e-5 and λ_{sample} = 1) in Fig. 4(d). The corresponding coil shape was # 8 in Fig. 1(d) (winding length: 358 mm, open angle: 91.3 degrees).

Figure 5 shows the evaluation factors for $|\boldsymbol{B}_0|$ = 6.5 mT. The dependence of the signal on λ_{sample} and λ_{coil} was similar to that in other $|\boldsymbol{B}_0|$ but the intensity was lower (Fig. 5(a)). R_{coil} (≤ 51.0 mΩ) was dominant compared to R_{sample} (≤ 24.3 μΩ) (Figs. 5(b) and (c)). The maximum SNR was 0.0232 and near the center region (λ_{coil} = 1 and λ_{sample} =1e-1) in Fig. 5(d). The corresponding coil shape (winding length: 407 mm, open angle: 108 degrees) was similar to # 4 (rather than # 5) in Fig. 1(d). Although R_{coil} was dominant compared to R_{sample}, the maximum SNR was not at the upper left region (λ_{coil} = 1e5 and λ_{sample} = 1e-5), suggesting that higher λ_{coil} (> 1) decreases $|B_1^-|$ and lower λ_{sample} increases R_{coil}.

Inductance and quality factor are also important indicators for coil. Figure 6 shows the inductance, $Q_{unloaded}$ (quality factor with unloaded condition), and Q_{loaded} (quality factor with loaded condition) dependence on λ_{sample} and λ_{coil} in the case of $|\boldsymbol{B}_0|$ = 7 T, 0.3 T, and 6.5 mT. We calculated the inductance by the following equation [31]:

$$L = sum\left(\begin{bmatrix} L_{11} & \cdots & L_{1n} \\ \vdots & \ddots & \vdots \\ L_{n1} & \cdots & L_{nn} \end{bmatrix}\right), \tag{15}$$

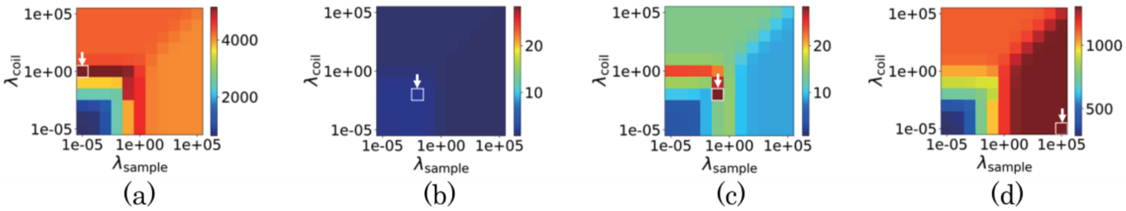

Fig. 3 Signal, noise and SNR dependence on λ_{sample} and λ_{coil} in the case of $|\boldsymbol{B}_0| = 7$ T. (a) Signal (a.u.). (b) Coil resistance (Ω). (c) Sample resistance (Ω). (d) SNR (a.u.). Plotted rectangular region indicated by the arrow corresponds to the maximum value.

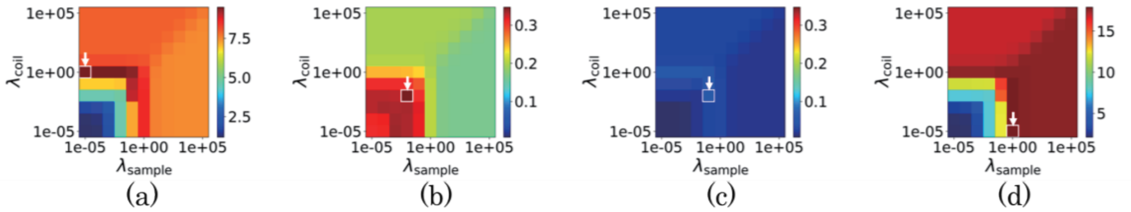

Fig. 4 Signal, noise and SNR dependence on λ_{sample} and λ_{coil} in the case of $|\boldsymbol{B}_0| = 0.3$ T. (a) Signal (a.u.). (b) Coil resistance (Ω). (c) Sample resistance (Ω). (d) SNR (a.u.). Plotted rectangular region indicated by the arrow corresponds to the maximum value.

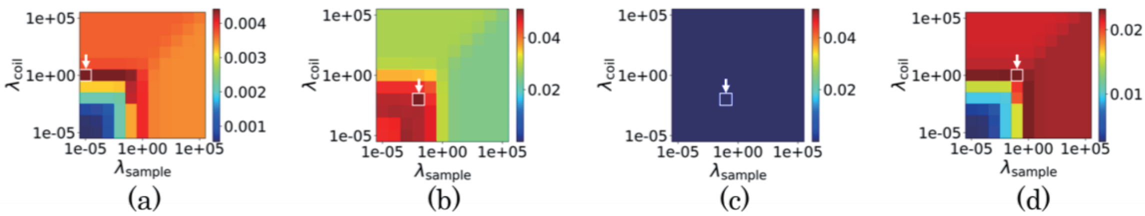

Fig. 5 Signal, noise and SNR dependence on λ_{sample} and λ_{coil} in the case of $|\boldsymbol{B}_0| = 6.5$ mT. (a) Signal (a.u.). (b) Coil resistance (Ω). (c) Sample resistance (Ω). (d) SNR (a.u.). Plotted rectangular region indicated by the arrow corresponds to the maximum value.

$$L_{ij}(i = j) = \frac{\mu_0 p}{2\pi}\left(ln\left(\frac{\mu_0 A}{pR}\right) + 0.25\right), \tag{16}$$

$$L_{\mathrm{ij}}(i \neq j) = \frac{\mu_0}{4\pi}\oint_{C_{\mathrm{j}}}\oint_{C_{\mathrm{i}}}\frac{d\boldsymbol{r}_{\mathrm{i}} \cdot d\boldsymbol{r}_{\mathrm{j}}}{|\boldsymbol{r}_{\mathrm{j}} - \boldsymbol{r}_{\mathrm{i}}|}, \tag{17}$$

where p is the perimeter of the coil, A is the area enclosed by the coil, R is the wire radius, C_{i} is the i-th coil path, $\boldsymbol{r}_{\mathrm{i}}$ is the position vector on C_{i}, and $\boldsymbol{r}$i is the unit vector along C_{i}. Note that in this calculation, the inductance does not depend on the frequency. We calculated the quality factors by the following equation [1]:

$$Q_{\text{unloaded}} = \frac{2\pi f_0 L}{R_{\text{coil}}}, \tag{18}$$

$$Q_{\text{loaded}} = \frac{2\pi f_0 L}{R_{\text{coil}} + R_{\text{sample}}}. \tag{19}$$

The optimal coil shape of 7 T, 0.3 T, and 6.5 mT (# 9, # 8, and the shape similar to # 4 in Fig. 1 (d)) had inductance of 0.30, 0.42, and 0.54 μH, Q_{unloaded} of 59.08. 24.11, and 154.25 (a.u.), and Q_{loaded} of 723.46, 24.11, and 180.62 (a.u.), respectively. Segmented capacitors are used for tuning and matching of a coil in the step of fabrication. For the making low-frequency coils, to increase the inductance considering the coil tuning, we can increase the number of turns by overwrapping the several windings at the location of current path determined by the proposed method.

Specific absorption rate (SAR) is also important parameter for safety regulation of power transmission especially for RF transmit coils [1]. However, our paper focuses on the receive coil and most of the papers regarding the receive only coil do not consider SAR [32].

We confirmed that the optimal λ_{coil} and λ_{sample} depend on the static magnetic field intensity of $|\boldsymbol{B}_0|$. The optimal coil shape for 7 T, 0.3 T, and 6.5 mT (# 9, # 8, and the shape similar to # 4 in Fig. 1 (d)) had the winding length of 285, 358, and 407 mm, and the open angle of 74.8, 91.3, and 108 degrees, respectively. This suggests that the coil shape achieving the optimal SNR in lower $|\boldsymbol{B}_0|$ become larger compared to that in higher $|\boldsymbol{B}_0|$ to enhance $Ave.(|B_1^-(ROI)|)$ by allowing an increase of R_{coil} and R_{sample}.

4. Conclusion

We proposed a novel method based on inverse problem

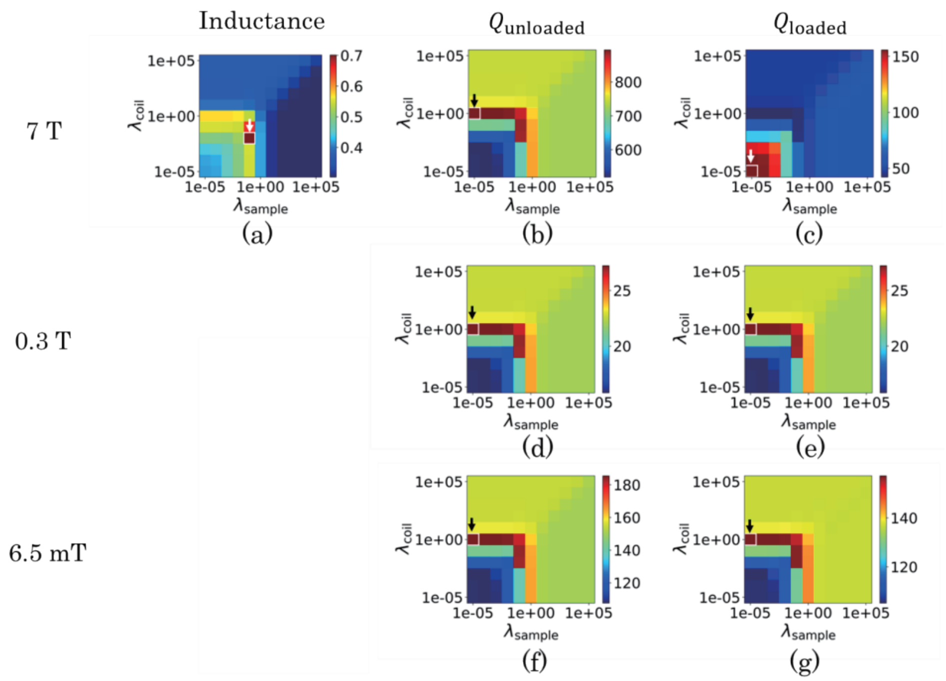

Fig. 6 Inductance, Q_{unload}, and Q_{load} dependence on λ_{sample} and λ_{coil} in the case of $|\boldsymbol{B}_0| = 7$ T, 0.3 T, and 6.5 mT. (a) Inductance (μH). (b) Q_{unload} (a.u.) and (c) Q_{load} (a.u.) in the case of $|\boldsymbol{B}_0| = 7$ T. (d) Q_{unload} (a.u.) and (e) Q_{load} (a.u.) in the case of $|\boldsymbol{B}_0| = 0.3$ T. (f) Q_{unload} (a.u.) and (g) Q_{load} (a.u.) in the case of $|\boldsymbol{B}_0| = 6.5$ mT. Plotted rectangular region indicated by the arrow corresponds to the maximum value.

analysis to design a single-channel RF receive coil with an optimized SNR in MRI scanner of a variety of static magnetic field intensity $|\boldsymbol{B}_0|$. We defined the objective function with terms related to the signal, coil resistance noise and sample resistance noise. By minimizing the function and evaluating the balance of two terms related to the noise, we obtained the optimal coil shape for $|\boldsymbol{B}_0|$ of interest in case that the ROI is rat kidney. The coil shape achieving the optimal SNR in lower $|\boldsymbol{B}_0|$ became larger compared to that in higher $|\boldsymbol{B}_0|$ to enhance $Ave.(|B_1^-(ROI)|)$ by allowing an increase of R_{coil} and R_{sample}.

In the future, we explore the configuration of our method to obtain the coil shape more suitable to each scanner configuration such as the direction of $|\boldsymbol{B}_0|$. For the target region, we will verify the potential expansion to other regions/organs rather than rat kidney for preclinical applications of small animals. In addition, we will conduct the comparison of the coil designed using proposed method with coils designed using other conventional methods by AC analysis using electromagnetic simulation and experimental evaluation.

Acknowledgements This work was supported by Suzuken Memorial Foundation and Next Generation Biomedical Measurement Research Network Program, The University of Tokyo supported by Nakatani Foundation, AMED (Japan Agency for Medical Research and Development) under Grant Number 23he0422030j0001, and JSPS KAKENHI Grant Number JP23H03721.

References

1) D. Hernandez and K.-N. Kim: *Investig. Magn. Reason. Imaging*, **24**, 95 (2020).
2) E. J. Baldelomar, J. R. Charlton, S. C. Beeman and K. M. Bennett: *Am. J. Physiol. Renal. Physiol.*, **314**, F399 (2018).
3) R. Watts and Y. Wang: *Magn. Reason. Med.*, **48**, 550 (2002).
4) S. M. Wright and L. L. Wald: *NMR in Biomedicine*, **10**, 394 (1997).
5) H. Takahashi, T. Dohi, K. Matsumoto and I. Shimoyama: Proc. MEMS 2007, 549 (2007).
6) Y. Wang: Principles of Magnetic Resonance Imaging: Physics Concepts, Pulse Sequences, & Biomedical Applications (CreateSpace Independent Publishing Platform, California, 2012).
7) D. I. Hoult: *Concepts. Magn. Reason.*, **12**, 173 (2000).
8) G. Giovannetti, A. Flori, D. D. Marchi, G. Matarazzo, F. Frijia, S. Burchielli, D. Montanaro, G. D. Aquaro and L. Menichett: *Concepts Magn. Reason. Part B Magn. Reason. Eng.*, **47B**, e21361 (2017).
9) M. D. Harpen: *Med. Phys.*, **14**, 616 (1987).
10) M. Takahashi, M. Fushimi, S. Yabukami, M. Sekino and A. Kuwahata: *AIP Adv.*, **14**, 015216 (2024).
11) S. E. Hurlston, G. P. Cofer and G. A. Johnson: *Int. J. Imaging Syst. Technol.*, **8**, 277 (1997).
12) A. Pohlmann and T. Niendorf: Preclinical MRI of the Kidney Methods and Protocols, Vol. 2216, pp.131-155 (Humana Press, New Jersey, 2021).
13) C. Constantinides, S. Gkagkarellis, S. Angeli and G. Cofer: 32nd Annu. Int. Conf. IEEE Eng. Med. Biol. Soc., 6657 (2010).

14) K. N. Kim, J. H. Seo, S. D. Han, P. Heo, G. H. Im, and J. H. Lee: *Scanning,* **37**, 361 (2015).
15) J.-H. Seo, Y. Ryu and J.-Y. Chung: *Sensors,* **22**, 4274 (2022).
16) R. Turner: *J. Phys. D: Appl. Phys.,* **19**, L147 (1986).
17) G. Shou, L. Xia, F. Liu, M. Zhu, Y. Li, and S. Crozier: *IEEE Trans. Magn.,* **46**, 1052 (2010).
18) B. G. Lawrence, S. Crozier, D. D. Yau and D. M. Doddrell: *IEEE Trans. Biomed. Eng.,* **49**, 64 (2002).
19) H. Fujita, S. M. Shmaryu, M. R. Thompson, M. A. Morich, L. S. Petropoulos, and V. C. Srivastava: *Int. J. Appl. Electromagn. Mech.,* **9**, 277 (1998).
20) H. Fujita, L. S. Petropoulos, M. A. Morich, S. M. Shvartsman and R. W. Brown: *IEEE Trans. Biomed. Eng.,* **46**, 353 (1999).
21) L. Tugan Muftuler, G. Chen and O. Nalcioglu: *Phys. Med. Biol.,* **51**, 6457 (2006).
22) D. K. Overson, J. Bresticker, D. Willey, F. Robb, A. W. Song, T. K. Truong, and D. Darnell: *Phys. Med. Biol.,* **68**, 125003 (2023).
23) A. Kumar and P. A. Bottomley: *Magn. Reason. Med.,* **56**, 157 (2006).
24) B. Gruber, M. Froeling, T. Leiner and D. W. J. Klomp: *J. Magn. Reason. Imaging,* **48**, 590 (2018).
25) J. P. Marques, F. F. J. Simonis and A. G. Webb: *J. Magn. Reason. Imaging,* **49**, 1528 (2019).
26) L. L. Wald, P. C. McDaniel, T. Witzel, J. P. Stockmann and C. Z. Cooley: *J. Magn. Reason. Imaging*, **52**, 686 (2020).
27) S. Shen, Z. Xu, N. Koonjoo and M. S. Rosen: *IEEE Trans. Biomed. Eng.,* **68**, 1106 (2021).
28) A. J. Mäkinen, R. Zetter, J. Iivanainen, K. C. J. Zevenhoven, L. Parkkonen, and R. J. Ilmoniemi: *J. Appl. Phys.,* **128**, 063906 (2020).
29) R. Zetter, A. J. Mäkinen, J. Iivanainen, K. C. J. Zevenhoven, R. J. Ilmoniemi, and L. Parkkonen: *J. Appl. Phys.,* **128**, 063905 (2020).
30) C. M. Collins and M. B. Smith: *Magn. Reason. Med.,* **45**, 692 (2001).
31) M. T. Thompson: *Power Control and Intelligent Motion*, Inductance Calculation Techniques-Part II: Approximations and Handbook Methods (1999).
32) A. M. Flynn, B. Lechêne, G. Scott, G. D. Reed, P. J. Shin, M. Lustig, and A. C. Arias: *Nat. Commun.,* **7**, 10839 (2016).

Received Dec. 04, 2023; Revised Jan. 04, 2024; Accepted Mar. 18, 2024

Journal of the Magnetics Society of Japan

Vol. 48 No. 3 (通巻第333号) 2024年5月1日発行

Vol. 48 No. 3 Published May 1, 2024
by the Magnetics Society of Japan
Tokyo YWCA building Rm207, 1–8–11 Kanda surugadai, Chiyoda-ku, Tokyo 101–0062
Tel. +81–3–5281–0106　Fax. +81–3–5281–0107

Printed by JP Corporation Co., Ltd.
Sports Plaza building 401, 2–4–3, Shinkamata Ota-ku, Tokyo 144–0054
Advertising agency: Kagaku Gijutsu-sha

発行：(公社)日本磁気学会　101–0062　東京都千代田区神田駿河台 1–8–11　東京YWCA会館 207 号室
製作：ジェイピーシー　144–0054　東京都大田区新蒲田 2–4–3　スポーツプラザビル401　Tel.（03）6715–7915
広告取扱い：科学技術社　111–0052　東京都台東区柳橋 2–10–8　武田ビル4F　Tel.（03）5809–1132